Journal of Fluids and Structures 137 (2025) 104340

Contents lists available at ScienceDirect

Journal of Fluids and Structures

journal homepage: www.elsevier.com/locate/jfs

# Achievements of *dense* ESPI *complex-valued* full-field *receptances* in experiment-based Rayleigh integral approximations of sound radiation from a vibrating plate

Alessandro Zanarini

*Dynamics & Vibrations of Machines, DIN – Industrial Engineering Dept., University of Bologna, Italy*

ARTICLE INFO

*Keywords:*
ESPI full-field technique
ESPI full-field frequency response functions
Experiment-based vibro-acoustic transfer functions
Acoustic pressure field simulation
Sound radiation of vibrating plates
Vibro-acoustics
NVH

ABSTRACT

Where can the exploitation of high spatial resolution optical full-field technologies – in *complex-valued* representation – bring, for an experiment-based extension of the Rayleigh integral approximation of sound radiation from a vibrating plate? *Dense receptance* maps may cope with the challenges of the most advanced Noise and Vibration Harshness (NVH) testing for the characterisation of the structural dynamics of the actual set-up, with damping and boundary conditions coming from the mounting and manufacturing, with all the potential delays of the responses caught around the superposition of a modally dense dynamics, but without the need of a Finite Element Model (FEM), especially in the case of lightweight structures. Sound radiations are explored in the *complex-valued* details of *vibro-acoustic transfer functions* and of *pressure* fields, by feeding the well-known Rayleigh formulation with Electronic Speckle Pattern Interferometry (ESPI)-based *receptances*, obtained from a simple thin rectangular plate, designed as a lightweight structure with a complex structural dynamics, its real constraints and damping characteristics. The contribution of *dense* experiment-based full-field *receptances* to the radiated sound fields at different distances is discussed in a broad frequency domain.

## 1. Introduction

The researchers may wonder where the exploitation of high spatial resolution optical full-field technologies can bring, especially for experiment-based *complex-valued* extensions of the Rayleigh integral approximation of sound radiation from a vibrating plate. This question is crucial also in raising the expected level and quality of the experiment-based benchmarks, against which the purely numerical simulation can be compared and tuned. *Complex-valued* ($\mathbb{C}$) quantities are therefore the only tools to deploy – in the frequency domain – the experiment-based achievements here proposed, because, with their data parts, they allow a clear description of real-life phenomena, not possible otherwise by *real-valued* ($\mathbb{R}$) quantities. In the formulations of this paper, the proper declaration of $\mathbb{C}$ quantities is underlined, while – if missing – the $\mathbb{R}$ nature is implicit. The driver of this work is the extensive usage of spatially *dense* experiment-based *receptances* in vibro-acoustics, in order to highlight the achievements in hybrid simulations with no numerical structural models. The *receptances* are obtained from full-field optical stroboscopic $\mathbb{C}$ ESPI measurements for their cleanest Operative Deflection Shapes (ODSs) (see Zanarini (2019a, 2020)), as the characterisation of the real vibrating structure in the whole frequency domain of interest, without any specific assumption, except for the linearisation of the real system's dynamic behaviour around the operative loading conditions. In this way, the experiment-based *receptances* substitute any numerical model of the structural domain (e.g. FEM), therefore overtaking the complex tuning of an artificial idealisation of the unknown vibrating part, because all the

*E-mail address:* a.zanarini@unibo.it.
*URL:* https://www.colorazeta.it/EngResearch/Zanarini_index_EN.htm.

https://doi.org/10.1016/j.jfluidstructs.2025.104340
Received 21 November 2024; Received in revised form 9 May 2025; Accepted 14 May 2025
Available online 25 June 2025

**Abbreviations**

| | |
|---|---|
| dof(s) | Degree(s) of freedom |
| DIC | Digital Image Correlation |
| EFFMA | Experimental Full-Field Modal Analysis |
| EMA | Experimental Modal Analysis |
| ESPI | Electronic Speckle Pattern Interferometry |
| FEM | Finite Element Model |
| FRAC | Frequency Response Assurance Criterion |
| FRF(s) | Frequency Response Function(s) |
| MAC | Modal Assurance Criterion |
| NAH | Nearfield Acoustic Holography |
| NVH | Noise and Vibration Harshness |
| ODS(s) | Operative Deflection Shape(s) |
| SLDV | Scanning Laser Doppler Vibrometer |
| $\omega$ | Circular frequency |
| $\mathbf{X_q}(\omega)$ | Structural displacement map |
| $\mathbf{F_f}(\omega)$ | Excitation forces |
| $\boldsymbol{H}_{d_{qf}}(\omega)$ | *Receptance* map |
| $\boldsymbol{V}_{af}(\omega)$ | Vibro-Acoustic FRFs |
| $\boldsymbol{p}(\boldsymbol{a},\omega)$ | Sound pressure map |

specifications of the materials, distributed damping, boundary conditions and loading patterns are already acquired from the test-rig's reality by the experiment-based *receptances*. Furthermore, the non-contacting full-field optical techniques add increased spatial detail, compared to more traditional lumped sensors like accelerometers or strain gauges. Full-field *receptances*, hardly matched for extremely *dense* patterns in the case of ESPI, are therefore able to carefully retain complex patterns in the ODSs without any inertia-related distortion, which is particularly important for lightweight components, such as shells and thin plates, as parts of a vehicle body, a fuselage, wings and generally screens.

This experiment-based approach is motivated because many times the sound radiation simulations from structural vibrations in NVH studies are run with linear structural finite or boundary element models (Kirkup, 1994; Desmet, 2004; Wind et al., 2006; Kirkup and Thompson, 2007; Richards et al., 2018; Kirkup, 2019; Conta et al., 2020), potentially simplified in the treatment of boundary conditions, frictions, damping, mistuning from actually produced parts and non-linearities. Similarly simplified structural models can also be found in studies about fluid–structure interactions (e.g., in the frequency domain, Lesoinne et al. (2001), Sandberg et al. (2009), Ohayon and Soize (2012), Vicente et al. (2015), Zhou et al. (2016)), where – however not the aim here – the focus is mainly on the fluid motion (e.g., in Dowell and Hall (2001), Kamakoti and Shyy (2004), Werter and De Breuker (2016), Li et al. (2017, 2019), Chen et al. (2019), Tian et al. (2021), Wang et al. (2022), Patil and Pitchaimani (2024)), rather than on the retaining of an extreme fidelity of the structural modelling, perfectly tuned with uncertainties, potential general damping (see Heylen et al. (1998), Ewins (2000)) and $\mathbb{C}$ eigenvectors. For the latter the tuning might be cumbersome (Wu et al., 2020; Mendez et al., 2021; Xu et al., 2021; Silva et al., 2021; Tsushima et al., 2021), the fluid motion being non-linear. In common simplifications, Experimental Full-Field Modal Analysis (EFFMA) does not contribute to any structural model and its updating. The approximation starts by forcing the damping to be only proportional[1] – if not neglected (Tsushima et al., 2017; Liu et al., 2024) – in a linear FEM (or functional solution by plates' theory with unverified constraints), yielding a $\mathbb{R}$ truncated modal base. When general damping is introduced for the formulation of the numerical structural model, the evaluations neutralise it (Bueno et al., 2015; Chen et al., 2017; Lokatt, 2017; Tian et al., 2024), reverting to unverified models. Sometime the investigations are focused only on a single tonal, or resonance, propagation (Takezawa et al., 2016), where just one eigensolution of the vibrating surface is used as the effective source of pressure fields, becoming another form of strong simplification, like in the truncation of the modal base above, neglecting the effective blending of the eigensystem at every frequency. The insights of Afonso et al. (2017), Abdelkefi (2016) confirm that simplified models may diverge – due to a lot of assumptions – from the real manufactured components. These parallel realities might not be easily tuned, also with extended model updating (Friswell and Mottershead, 1995; Calvi, 2005; Zanarini, 2019b), thus being unfaithful. Instead, working with experiment-based full-field *receptances*, coming from broad frequency band testing, may represent a viable path in order to have the best achievable representation of the real behaviour of manufactured and mounted components, linearised around their working load levels, also with modally *dense* structural dynamics and complex patterns in the dynamic signature of the excitations.

[1] Note also that – as in Numerical study on gust energy harvesting with an efficient modal based fluid–structure interaction method – the damping matrix might be first declared as non-proportional to mass and stiffness matrices – therefore needing $\mathbb{C}$ eigenvectors and related maths for the further diagonalisation – but later wrongly misinterpreted as proportional for the simplicity of the formulation it can bring.

At their earlier steps, optical full-field measurements – based on analogue/chemical compounds – were mostly qualitative and not competitive in terms of time-to-result (Rastogi, 1997), until the advent of digital sensors started – with limited amounts of processed data – to open new perspectives. They were therefore mainly used to depict the response shape of a structure at a particular frequency of interest, due to the high spatial sampling offered and high consistency of each measurement degree of freedom with neighbouring locations (Kreis, 2004). Their output was, since the beginning, a highly detailed spatial domain at few frequencies, while traditional sensors (strain gauges or accelerometers) could give only a coarse spatial representation, obtained by their lumped placement. However, with surface ODSs rapidly changing from frequency to frequency, as function of the complex superposition of the underneath eigensolutions in non-conventional patterns, the early optical full-field measurements started to release relevant information on where to better locate the lumped vibration sensors or strain-gauges, the only quantitative broad frequency band instruments at the time.

But, since the 1980s, the Scanning Laser Doppler Vibrometer (SLDV) approach has expanded the technique of contact-less single point measurement in time/frequency domains to a finer grid of locations than with traditional sensors. Due to the scanning of a generalised locations' grid, where the points might be also uncorrelated in distinct patches, the SLDV can be defined as an optical *non-native* full-field digital instrumentation. This has extended the concept of the velocity sensors to a spatially more detailed acquisition, also without adding inertia to the surface of the specimen under dynamic test. Remarkable were the results with SLDV in Stanbridge and Ewins (1999), Warren et al. (2011), especially in the continuous scanning LDV (CSLDV) attempts in Stanbridge et al. (2004), Allen and Sracic (2010), Di Maio and Ewins (2011), Giuliani et al. (2013), Ehrhardt et al. (2017), Di Maio et al. (2021) by driven mirrors and polynomial-based data processing. Thus SLDV was until recently considered the reference for the need of spatially detailed Frequency Response Function (FRF) measurements in NVH, because SLDV has kept the same peculiarities of previous technologies and proven procedures, avoiding inertia-related issues, just adding more degrees of freedom (dofs) at a reasonable cost.

Optical full-field technologies, based instead on an imaging sensor that acquires photons altogether – not with a delayed scan, normally in an even denser grid than that of SLDV – in the whole matrix of light sensible sites, can be called *native*, as well as *image-based*. They approach the measurement from another point of view, that of the acknowledged quality obtainable in the spatial domain, especially in terms of consistency and continuity of the deflection field in the neighbouring dofs, as proved earlier by Van der Auweraer et al. (1999, 2000). Among optical *native* full-field technologies, after the first trials (Van der Auweraer et al., 1999, 2000, 2001) by pulsed coherent laser light, stroboscopic ESPI has given – by working in the frequency domain with $\mathbb{C}$ quantities – since the early 2000s (Steinbichler and Gehring, 1996; Graham et al., 1999; Van der Auweraer et al., 2002; Leval et al., 2005) an extremely accurate displacement field at the frequency of interest up to several kHz; but having data at all the lines of a broad frequency band can be prohibitive, due to time-consuming stepped sine excitation/acquisition, not fully automated up to now, even with the latest advancements in the high-speed image sensors as in Meteyer et al. (2021). Therefore, ESPI is more suited to laboratory – or controlled environments – measurements, typical of research projects (Steinbichler and Gehring, 1996; Graham et al., 1999; Van der Auweraer et al., 2002; Leval et al., 2005; Zanarini, 2018, 2019a). High-speed Digital Image Correlation (DIC)[2], with its first commercial prototypes since around 2005, has good detail in the time resolved displacement maps, although the extraction of the correlated fields can be demanding in terms of calculation time. DIC can be more limited in the frequency domain, as the sensor/electronics bandwidth puts a trade-off between resolution and sampling rate, together with some limitations on the cameras' memory capacity, although nowadays relevant electronics improvements have been made. However, DIC technology has shown interesting in-situ applications (Baqersad et al., 2017; Wang et al., 2011a,b; LeBlanc et al., 2012; Ehrhardt et al., 2017), exploiting the greater flexibility, but lower accuracy, of the technique also outside controlled set-ups. As the experiment-based optical full-field testing has clearly proved in Zanarini (2019a, 2020, 2022a) to be consistent in releasing high spatial resolution dynamic ODSs with reduced amount of noise on the fields, this paper is therefore focused on sound radiation numerical simulations from a vibrating surface, with a specific attention to ESPI-based datasets. The latter are used at their highest spatial resolution, or native *dense* resolution – on which no reducing interpolation was applied by topology transforms, and with broad frequency band content. The ESPI-based datasets give, up to now[3] and according to Zanarini (2019a, 2020), the cleanest displacement fields, therefore becoming a valuable candidate in non-contacting experiment-based sources of surface motion, to be explored in the approximation of the sound radiation, especially in the case of lightweight structures or panels. This brings a very high-quality source of full-field *receptances* to the vibro-acoustics' analyses thereafter.

The following notes can show the progressive growth of activities about full-field measurements by the author, which are involved in the achievements of this paper, and are based especially on the fundamental research TEFFMA[4] project. The latter aimed at making a comparison between the state-of-the-art in *native* full-field technologies (ESPI and DIC) with the *non-native* SLDV as reference, to

[2] The reader can find methodological references about DIC in Sutton et al. (2009), Bornert et al. (2009), Helfrick et al. (2011), Jones and Iadicola (2018).

[3] Recently, but about ten years later than the measurements at the core of this work, new comparisons appeared in O'Donoughue et al. (2023), confirming the qualities of ESPI. However, those measurements lead to no *receptances* for the approach here proposed. Furthermore, high-speed cameras in coherent light imaging (see Meteyer et al. (2021)) are trying – with further work to be made to reduce the redundant time-domain data – to overtake the more traditional issues of accurate stroboscopic ESPI (with phase-shifting as in Vrooman (1991), de Groot (1995), Huntley (1998), Lopes et al. (2014, 2019)), which remained the long lasting measurements for broad frequency band $\mathbb{C}$ results, later hinted in Section 2.1.1.

[4] A. Zanarini, scientific proposer & experienced researcher in the project TEFFMA – Towards Experimental Full Field Modal Analysis, funded by the European Commission – Marie Curie FP7-PEOPLE-IEF-2011 PIEF-GA-2011-298543 grant, and carried out by the author at Vienna University of Technology, Austria, on 1/02/2013–31/07/2015.

understand if these experimental procedures for standing broad frequency band structural vibrations – not fully mature but in progressive development – can provide NVH applications with enhanced peculiarities. Note that all the TEFFMA-related activities were based on the early findings of the *Speckle Interferometry for Industrial Needs*[5] project. The earliest presentations of TEFFMA works appeared in 2014 (Zanarini, 2014a,b), followed by consolidated reports[6] in 2015. In Zanarini (2018) a gathering of the TEFFMA project's activities was firstly attempted, while in Zanarini (2019a) an extensive description of the whole full-field *receptance* estimation was faced and in Zanarini (2019b) the EFFMA was detailed together with full-field modeshapes-based model updating attempts. The works in Zanarini (2020) underlined the quality of *native* full-field datasets – ESPI and DIC – in broad frequency band dynamic testing. In Zanarini (2022a) a precise comparison was made about new achievements for rotational and strain FRF high resolution maps. In the recent paper (Zanarini, 2022b) the variability of fatigue failure risk maps, obtained from ESPI-based datasets (reduced at the SLDV references) and fatigue spectral methods, was introduced by the changes in the $\mathbb{R}$ amplitude of the excitation dynamic signature, followed[7] by further refinements. With a recent work[8] the risk index mapping is addressed, instead, by means of DIC-based full-field *receptances* at the moderate (interpolated) resolution of SLDV in both spatial and frequency domains, while with (Zanarini, 2024b) the analysis is made with the original DIC dataset, without any potential distortion coming from the topology transforms and related down-sampling interpolations. Another relevant addition in Zanarini (2024b,c) is the use of $\mathbb{C}$ coloured noises – instead of the $\mathbb{R}$ ones in Zanarini (2022b,c, 2023a, 2024a) – as excitation signals with potential randomness in the *complex amplitude* and *phase*, as is here inherited by the modelling of Section 4.

The earlier works (Zanarini, 2022c, 2023a) on direct vibro-acoustics explored the feasibility of the Rayleigh sound radiation integral approximation by means of full-field receptances, with an ESPI-based dataset, but reduced to the lower resolution of the SLDV references. Furthermore, Zanarini (2023b) addressed the problem of error propagation in vibro-acoustics, once the error is scattered on full-field *receptances*, particularly manifest in SLDV-based datasets. In Zanarini (2024a) can be found the author's first attempt to use full-field *receptances* also in pseudo-inverse vibro-acoustics, but with a relatively low spatial resolution – with DIC as measurements, but SLDV as geometry and frequency references – with 2907 structural dofs, 2601 acoustic dofs and 1285 frequency lines. The relatively small size of the vibro-acoustic problem in Zanarini (2022c, 2023a,b, 2024a) also permitted some tentative implementations of parallel processing of the diffusion matrix between the structural and the acoustic domains, to speed up the calculation time, at the expense of a broader memory allocation (145 GB). The full parallelisation is not feasible here under the constraint of 192 GB of physical allocable memory in the available workstation, instead, due to the ESPI dataset in its *native dense* resolution with 49042 structural dofs and 40401 acoustic dofs, 1285 frequency lines, as documented in Sections 2 and 5.

Different works were therefore published by the author, following the EC-funded projects, about the growing full-field optical technologies, their advantages and drawbacks in a broad scenario of applicability and perspectives. It was shown, especially in the latest works from the TEFFMA project and from its spin-off[9] researches, how the growing *native* full-field techniques have started to offer tangible advances for the consistency and continuity of their data fields, with clear repercussions in EFFMA[10] and model updating, in vibro-acoustics[11] and in derivative calculations (rotational[12] dofs, strains, stresses, risk index[13] maps). Optical technologies can therefore, more and more frequently, cope with the challenges of the most demanding structural testing without the need of a FEM, like sensing, across a broad frequency range, the full-field *receptance* maps. The latter become useful to characterise, in the space and frequency domains, the specific structural dynamics of the actual set-up, with all the potential delays of the responses, caught around the superposition of a modally dense dynamics and hardly modellable damping or boundary conditions. Indeed, the experiment-based full-field optical *receptances* can advance, extend and raise the level of the benchmarks, needed by any NVH numerical tool, to improve the design procedures of prototypes and manufactured components.

[5] HPMI-CT-1999-00029 Post-doctoral Marie Curie Industry Host Fellowship project at Dantec Ettemeyer GmbH, Ulm, Germany, in 2004-5. Since the early ESPI-related testing, full-field optical measurements gave relevant and hyper-detailed mapping about the local behaviour for enhanced structural dynamics assessments and fatigue spectral methods. In particular, for stroboscopic ESPI, see: Dynamic Behaviour Characterization of a Brake Disc by means of Electronic Speckle Pattern Interferometry Measurements; Full field ESPI measurements on a plate: challenging experimental modal analysis; Fatigue life assessment by means of full field ESPI vibration measurements; Full field ESPI vibration measurements to predict fatigue behaviour.

[6] See in Proceedings of the ICoEV2015 International Conference on Engineering Vibration: Comparative studies on full field FRFs estimation from competing optical instruments; Accurate FRFs estimation of derivative quantities from different full field measuring technologies; Full field experimental modelling in spectral approaches to fatigue predictions; Model updating from full field optical experimental datasets.

[7] The effects of different excitation locations are shown in About the excitation dependency of risk tolerance mapping in dynamically loaded structures. Both aspects – of amplitude modulation and location of the excitation – are gathered in Risk tolerance mapping in dynamically loaded structures as excitation dependency by means of full-field receptances.

[8] See Exploiting DIC-based full-field receptances in mapping the defect acceptance for dynamically loaded components.

[9] The present work, together with Zanarini (2022b,c, 2023a,b, 2024a,b,c), can be considered a spin-off research activity in the wake of the TEFFMA project, because altogether they have introduced advances and novelties that were not included specifically at the end of it, in particular about the failure risk index mapping (Zanarini, 2022b, 2024b) and the vibro-acoustics (Zanarini, 2022c, 2023a, 2024a, 2023b, 2024c), both obtained from its full-field *receptances*.

[10] See Van der Auweraer et al. (2001), Zanarini (2014a,b, 2018, 2019a,b, 2020, 2022a) for extending Experimental Modal Analysis (EMA) to EFFMA, enhanced structural dynamics assessments and model updating.

[11] See specifically (Zanarini, 2022c, 2023a,b, 2024a,c) for vibro-acoustics.

[12] In Zanarini (2018, 2022a) the reader can specifically appreciate the effect of the measurement noise on the estimation of rotational dofs; however, unfortunately due to the complexity or burden of their measurement, the rotational dofs are usually disregarded, whilst they are relevant for the successful build of a reliable dynamic model for complex structures (Heylen et al., 1998; Liu and Ewins, 1999; Research network, 1998; Ewins, 2000; Friswell and Mottershead, 1995; Haeussler et al., 2020).

[13] See instead (Zanarini, 2022b, 2024b) for enhancements in the mapping from fatigue spectral methods and failure risk grading.

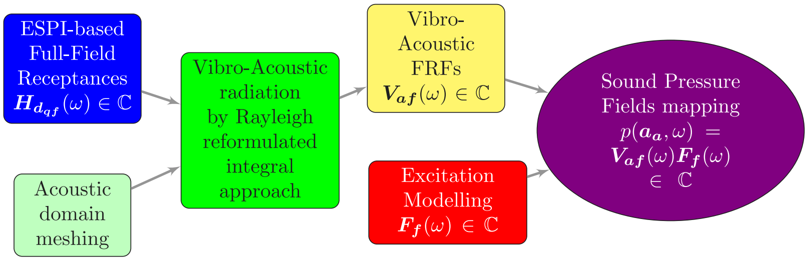


**Fig. 1.** Overview of the steps for the sound pressure fields mapping in direct vibro-acoustics.

This work, following the sketch in Fig. 1, exploits therefore the ESPI-based *receptances'* dataset with its dense resolution in the spatial and frequency domains for an accurate experiment-based characterisation of the vibrating structure, as briefly detailed in Section 2 by means of a recall of the experiment-based FRF modelling, while a brief description of the testing is outlined in Section 2.1, with attention to the set-up, and hints at the stroboscopic $\mathbb{C}$ ESPI measurements in Section 2.1.1.

To address the hybrid and direct vibro-acoustic modelling with high accuracy in both the spatial and frequency domains, the well-known Rayleigh integral approximation is re-elaborated in Section 3 – in a $\mathbb{C}$ matrix formulation – for allowing the use of ESPI-based full-field *receptances* and of broad frequency band *excitations* instead of the more common surface *velocities*, to obtain the *vibro-acoustic transfer matrices* – as energy injection location dependent – and the *pressure* fields – as excitation spectra dependent.

Section 4 is therefore dedicated to the formulation of coloured noises in a broad frequency band, with potential randomness in the *complex amplitude* and *phase*. The proposed formulation can represent any signal, from the simpler $\mathbb{R}$ and noise-free excitation to the more adherent signal to natural excitation, like signals with randomness in the *complex amplitude* and *phase*.

Section 5 contains all the simulations and notes about the direct vibro-acoustic problem, with examples given in the space and frequency domains, after notes on the meshing of the acoustic domain, at different distances of the acoustic mesh from the vibrating plate, while varying the excitation model of Section 4. Special attention is given to the multi-modal superposition, specifically manifest outside the eigenfrequencies by complex patterns in the ODSs, and to the contribution of the experiment-based full-field *receptance maps* to the accuracy of the radiated *acoustic pressure* over *force FRFs* and *pressure* fields.

The reader's attention is finally drawn to Section 6 for the final comments. The Abbreviations' panel complements the reading for recurrent acronyms.

## 2. Methods: experiment-based full-field *receptances*

As widely anticipated in Section 1, the impedance-based studies, by means of full-field optical measurements, in the TEFFMA project were the pivot of all the activities. The available technologies were thoroughly investigated to achieve highly reliable full-field FRFs with unprecedented spatial and frequency resolutions, for any further speculation that may come either from real testing or from numerical models, also in hybrid frameworks, like those of Transfer Path Analysis (TPA) (Wagner et al., 2020; Mueller et al., 2020; Haeussler et al., 2020), or like here for full-field hybrid vibro-acoustics. The ***bold*** notation of the following math expressions refers to arrays/vectors of multiple components, while *plain text* pertains to a single component only.

### 2.1. Brief summary of the testing in the TEFFMA project

A brief[14] summary of what was available at TU-Wien as in Fig. 2 can be highlighted: a dedicated seismic/floating floor room with an anti-vibration table; a mechanical and electronic workshop with technicians at disposal; traditional tools for vibration and modal analysis, like shakers and impedance heads; but, in particular, there were 1D SLDV (dated around 2003), 3D Hi-Speed DIC (dated around 2008, with an external high-frequency high-power lighting system, active in Figs. 2*a*, *b*) and stroboscopic 3D ESPI (dated around 2004 for the $\mathbb{C}$ stepped sine processing prototype as hinted in Section 2.1.1, but with a hi-resolution head from 2008 in Fig. 2*c*, with its functional scheme in Fig. 2*d*) optical full-field measurement instruments as gathered for the concurrent testing in Fig. 2*a*. Note that the vibrating plate is placed far enough away from the closest reflecting surface (the wall on the back, visible at the very top of Fig. 2*a*, was around 1.5 m distant), to consider the potential sound reflections as meaningless[15] in the frequency range of interest, therefore appropriate for the Rayleigh integral approximation – which theoretically requires an infinite baffled surface, with no other pressure sources – later used for the sound radiation simulations, as in Section 3.

[14] The reader can find the most detailed notes on the test campaign in Zanarini (2019a), with further suggestions in Zanarini (2019b, 2020, 2022a, 2024b,c).

[15] The interested reader can see in the Tab.1 of Zanarini (2023b) an example of tabulated Green's diffusion function contributions, in terms of frequency and distance: the amplitude of the back-reflected contributions with a 3 m travelling distance is 4 orders of magnitude lower than that at 1 mm at 20 Hz, but this strongly drops to 31 orders of magnitude lower at 1024 Hz, therefore clearly with minimal relevance to the plate dynamics. Also the shakers' membranes in Fig. 2*b* may have a limited contribution, but already accounted for during the sine stepped excitation in ESPI measurements as in Section 2.1.1, when the *Coherence functions* (Heylen et al., 1998; Ewins, 2000; Bendat and Piersol, 2000) as in Zanarini (2019a), in their high quality, addressed the excitation as coming from the active shaker head only.

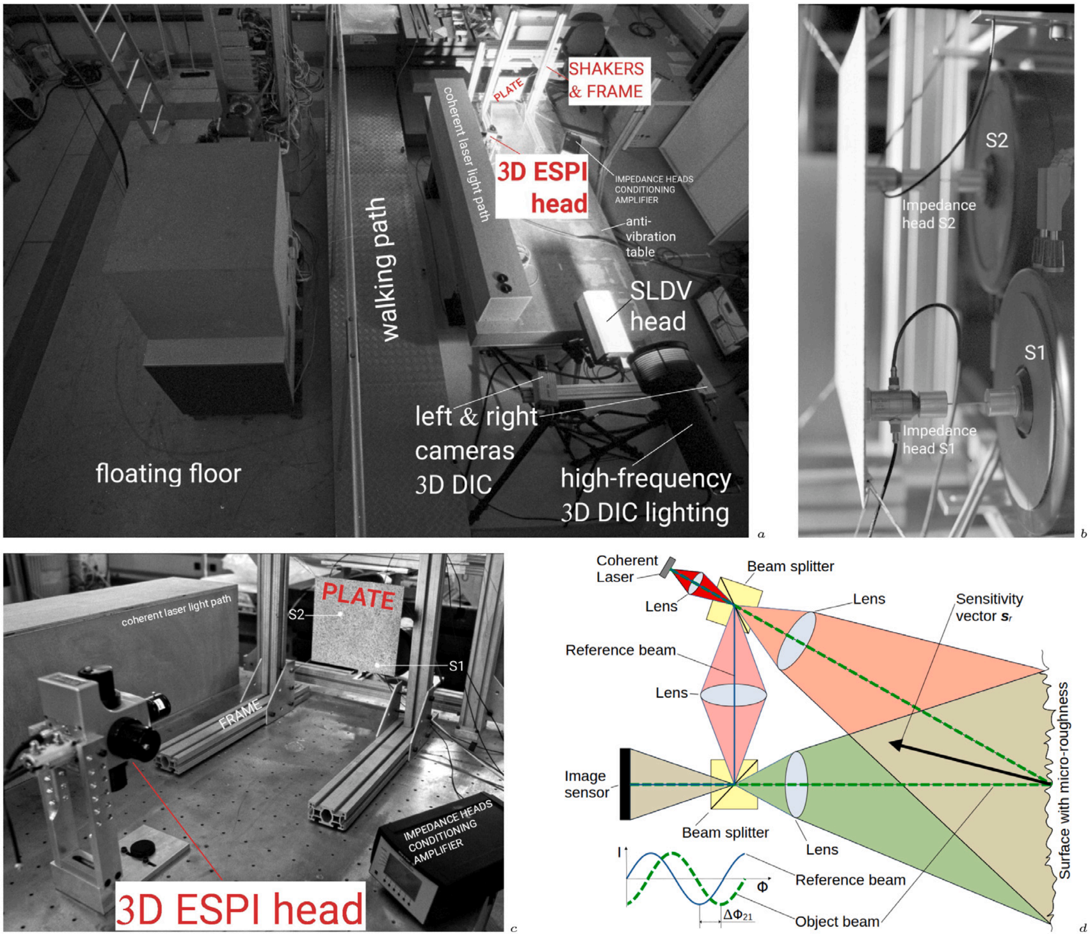


**Fig. 2.** The test-rig in the TEFFMA project's laboratory (see Zanarini (2014a,b, 2018, 2019a,b, 2022a)) for the concurrent full-field testing of SLDV, DIC & ESPI: aerial view in *a* with ESPI head on a side, to let the SLDV & DIC techniques acquire the measurements; close-up on the 2 shakers with their impedance heads on the back of the plate in *b*; close-up on the ESPI head in its working position in front of the restrained plate sample in *c*; in *d* the scheme of the ESPI head is proposed. (For the best interpretation of the colours in the figure(s), the reader is referred to the web or PDF version of this article).

Accurate studies were needed to understand each technological limit and if a common test for concurrent usage might be really possible by these very different measurement techniques. All this brought to a unique set-up for the comparison of the 3 optical technologies in *full-field FRF* estimations at each maximal manageable resolution, in the trade-off between the broad frequency range of interest and the highest quality achievable. Great attention was paid to the design of experiments for further research in modal analysis, structural dynamics and NVH, as spin-off researches (Zanarini, 2022b,c, 2023a,b, 2024a,b,c) documented. The accurate tuning of the rig and of the instruments brought a feasible performance overlapping directly out of each technique, reminding the reader that the same structural dynamics can be sensed in complementary domains, which means frequency for SLDV and ESPI, time for DIC. Topology transforms, as extensively detailed in Zanarini (2019a, 2022a), were added whenever a quantitatively comparison of the datasets[16] was needed in the same physical references of geometry and frequency spacing.

The sample was a thin 7075-T6 aluminium alloy (elastic modulus $E$ = 71.7 GPa, Poisson ratio $\nu$ = 0.33) rectangular plate (external dimensions: 250 $x$ 236 $x$ 1.5 mm), which was fixed by wires to a rigid frame on the air-spring optical table (see Fig. 2*c*) to restrain any excessive rigid-body movement. Specifically, note that the specimen under test was designed as a lightweight structure to retain a complex and tightly-coupled structural dynamics – with its real constraints and damping characteristics – within the operative ranges of the used measurement technologies in the TEFFMA project. The flat plate was in pristine conditions, not to confuse the measurement errors with part's defects. The front-side of the plate presented a layer of paint with a DIC-friendly random noise pattern. The excitation was given by 2 electrodynamic shakers orthogonally positioned on the back-side of the plate, to fulfil

[16] The super-imposable datasets – to assure the maximal qualities in the measurements – were restrained to the following sets of (spatial grid dofs, frequency lines): (57 × 51, 1285) for SLDV (see Zanarini (2018, 2019a)), (111 × 108, 2008) for DIC (see Zanarini (2024b,c)) and (226 × 217, over 2000) for ESPI (see details in Zanarini (2019b) and settings in Section 2.1.1). ESPI dofs were roughly 4× DIC's ones, 16× SLDV's ones.

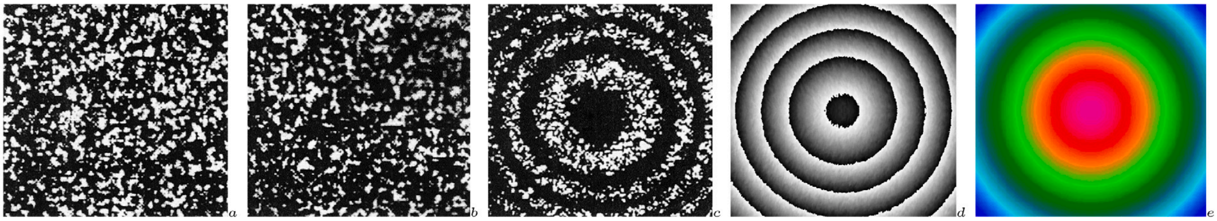

**Fig. 3.** An example of the basic steps of *speckles'* processing in ESPI chain: reference *interferogram* in *a* from Eq. (1), *interferogram* from a deformed state in *b* from Eq. (2), *fringes* in the *specklegram* of *c* from Eq. (3), *wrapped phase map* in *d* after *specklegram* processing and *unwrapped phase map* in *e*, projected for continuous out-of-plane displacement field as in Eq. (6).

the stepped-sine phase-shifting acquisition procedure for ESPI with an external sine waveform generator, while LMS Test.Lab system drove the shakers in SLDV and DIC measurements. Although ESPI and DIC could have sensed in-plane displacements thanks to their 3D nature, nothing – except meaningless noise – was measured above the sensitivity threshold, due to the specific geometry of the sample and orthogonal excitations. Therefore, the present work is only focused on out-of-plane vibrations of flat surfaces. The force signals were sampled at the shaker-plate interfaces by means of the force cells in the impedance heads (see Fig. 2*b*), to calculate the *receptances* $\boldsymbol{H}_{d_{qf}}(\omega)$ in Eq. (8).

### 2.1.1. Basics of stroboscopic complex-valued ESPI measurements

Note that stroboscopic ESPI was here used to measure the displacement maps $\mathbf{X}_{\mathbf{q}}(\omega)$ in the frequency domain. Therefore, a brief recapitulation from earlier works of the author, as already seen in footnote 5, might be of help to the reader, who can find broader contents in the highlighted references.

In ESPI the so-called *speckles* (see Doval (2000), Rastogi (1997)) are the result of statistical interference light intensity patterns, or *interferograms*; the latter are made by the superposition of the reference light wave front and the object light distribution, which is back-scattered by a surface with micro-roughness – the source of randomness, being illuminated by the same light through a beam-splitter, as in Fig. 2*d*. A simple mapping, in the sensor coordinates (u,v) as in Doval (2000), of the *interferograms* intensity $I(u,v)$ – taken in two distinct recordings – follows:

$$I_1(u,v) = I_0(u,v)\,[1 + \zeta(u,v)cos\,(\phi(u,v))] \in \mathbb{R}, \tag{1}$$

$$I_2(u,v) = I_0(u,v)\,\left[1 + \zeta(u,v)cos\,\left(\phi(u,v) + \Delta\phi_{21}(u,v)\right)\right] \in \mathbb{R}, \tag{2}$$

where $I_0(u,v)$ is the Bessel type *average radiance* between the object and reference wave fronts; $\zeta(u,v) \in [0,1]$ can be called the *complex degree of coherence*; $\phi(u,v)$ is the sum of the random phase noise component and the variation between the object and the reference phase difference; $\Delta\phi_{21}(u,v)$ is the deterministic phase difference induced by surface generalised deformation between two recordings. Examples of Eqs. (1),(2) are sketched in Fig. 3*a*, *b*, respectively. A well suited light source is that of a monochromatic laser with high coherence length, for which the photons in the ray keep the same phase lag for long paths – compared to the wavelength – to have no influence on the *speckles*, the signal carriers, therefore on the measurements. *Specklegrams* are instead maps, with the typical isolines called *fringes*, of phase difference between the different records of *speckles*, e.g. simply by $I_2(u,v) - I_1(u,v)$ from Eqs. (1),(2), as recalled as follows and as sketched in Fig. 3*c*:

$$I_1(u,v) - I_2(u,v) = I_0(u,v)\zeta(u,v)sin\left(\phi(u,v) + \frac{\Delta\phi_{21}(u,v)}{2}\right)sin\left(\frac{\Delta\phi_{21}(u,v)}{2}\right) \in \mathbb{R}. \tag{3}$$

Thanks to the constant wavelength of the coherent laser light, the *fringes* in the *specklegrams* are related to the difference in the optical paths of the light beams, thus to the deformation states of the object between the records. Many image-based enhancing techniques might be used to optimise the *fringes* in the *specklegrams*, to be later processed for obtaining the so called wrapped phase difference map, as exampled in Fig. 3*d*. The resolution of the sensor plays an important role in the ability to solve busy *specklegrams*. Different procedures can be used to quantitatively extract the unwrapped $\Delta\phi_{21}(u,v)$ from the enhanced *specklegrams* and Eq. (3), based on digital filtering and phase demodulation as in Ochoa et al. (1999), Georgas and Schajer (2012), or based on phase shifting as in Maas (1991), Vrooman (1991), Schreiber and Bruning (2007) dealing with other phase shifted recordings, or spatial Fast Fourier Transform filtering, as suggested in Kreis (2004) with related system design requirements.

Note that any $\mathbb{R}$ (u,v) map, whose ordinate values at each (u,v) location are represented in a *complex plane* with *real* and *imaginary* axes, appears as a line, angled with a measurement specific phase regarding the *real* axis, but with all the dofs-related segments laying on the same straight line, passing from the origin, with only two possible sides; the measurement of the whole map makes the projection of all the dofs-related segments on the *real* axis, always keeping the same relative sign among the dofs. Instead, a $\mathbb{C}$ (u,v) map on the *complex plane* appears like a cloud with relevant *complexity*, or relative thickness (full *complexity* pertains to a round shape), due to the potential spreading of the dofs' components in all the directions with different relative angles. When projected to the *real* axis for a measurement, the relation among the dofs is strongly dependent on the projecting angle, possibly leading – in this application – to misunderstandings about the sensed structural dynamics in tough scenarios.

In case of static defection shapes, $\Delta\phi_{21}(u,v)$ is merely $\mathbb{R}$, therefore any distinct recording may be enough to quantitatively extract the unwrapped $\Delta\phi_{21}(u,v)$ from the enhanced *specklegrams* and Eq. (3). Instead, if $\Delta\phi_{21}(u,v) \in \mathbb{C}$ as generally can be in dynamic ODSs, more attention should be paid in the selection of the recordings, as any time averaging[17] would destroy the *complexity* of the data field. The continuous wave of a coherent laser light can be made stroboscopic by means of an acousto-optical demodulator, which extracts the first harmonic at the same circular frequency $\omega$ of the sine excitation, as follows in Section 2.2. The stroboscopic illumination – being preferable for steady events such as harmonic responses due to its very high stability – can freeze the *interferogram* between two phases, or time delays, of the driving sine excitation, permitting the regular evaluation of the phase map $\Delta\phi_{k(k-1)}(u,v) \in \mathbb{R}$ between a reference record $k-1$ and the $k$th generic delayed record by a selectable phasing quantity $\Delta\Phi_k/\omega$, where $\Delta\Phi_k$ is influenced by the throughput of the sensor's electronics. Granted that a needed time delay $\Delta\Phi_0/\omega$ is due to the electronics speed at $\omega$, it is possible to run $K$ successive measurements by shifting the acquisition timing by adding a multiple of $2\pi/K$ to $\Delta\Phi_0$, so that the phase shifting becomes $\Delta\Phi_k = \Delta\Phi_0 + k2\pi/K$, with $k = 1 \dots K$. There results a series of $K$ equally phase-delayed events at the same circular frequency $\omega$ of the harmonic excitation. Even if the acquisitions $\Delta\phi_{k(k-1)}(u,v)$ belong to different positions on the steady harmonic response, $\Delta\Phi_0$ being common, they can be regrouped as belonging to the same virtual harmonic wave, each of them delayed from the other by the known quantity $2\pi/K$, and modelled as:

$$\Delta\phi_{k(k-1)}(u,v) = \boldsymbol{a}(u,v) + \boldsymbol{b}(u,v)cos[\boldsymbol{c}(u,v) + k2\pi/K] \in \mathbb{R}, \tag{4}$$

with a threshold value $\boldsymbol{a}(u,v)$ and a cosine wave of *complex amplitude* $\boldsymbol{b}(u,v)$ and *complex phase* delay $\boldsymbol{c}(u,v)$, relative to the cosine excitation with circular frequency $\omega$. By means of a non-linear least squares fitting, the $K$ phase maps in Eq. (4) are used to evaluate the parameters $(\boldsymbol{a}(u,v), \boldsymbol{b}(u,v), \boldsymbol{c}(u,v))$ to finally obtain $\Delta\phi_{21}(u,v) \equiv \Delta\phi_\omega(u,v) \in \mathbb{C}$, with its $\mathbb{C}$ parts at $\omega$ as:

$$\Delta\phi_\omega(u,v) = \{\boldsymbol{b}(u,v)cos[\boldsymbol{c}(u,v)], \boldsymbol{b}(u,v)sin[\boldsymbol{c}(u,v)]\} \in \mathbb{C}, \tag{5}$$

while the term $\boldsymbol{a}(u,v)$ is used to assess the proper shifting between the first and second exposures. This fitting of the harmonic signals reduces the noise in the fields. The same approach is followed by the external channels of more traditional sensors, synchronised with the ESPI exposures, like accelerometers or force cells, as was made since the works in footnote 5. The evaluation of the simple $\mathbb{R}$ data as in Eq. (4) can be heavily influenced by the phase delay between the excitation and the illumination, like exploring how heavily the $\mathbb{R}$ projection of $\mathbb{C}$ data can change with high *complexity* by such phase delay. Furthermore, the resolvable *fringes* in each map of Eq. (4) put a hard trade-off between final displacement and sensor resolution. Instead, the results in Eq. (5) at the specific frequency are independent of the single acquisition's parameters, delivering the whole $\mathbb{C}$ data field, in which some areas might have relative phase delays with the rest of the field (appearing as smooth gradients of the *complex phase* of the field), which is something never visible from Eq. (4) only, but extremely relevant for advanced EFFMA with closely-spaced or repeated eigenshapes and frequency dependent enquiries of general damping or anisotropies in structures. Furthermore, by Eq. (5) an extension (or nearly $\times K$ multiplication, with $K = 12$ in the TEFFMA project) of the measurable *complex amplitude* is obtained, which might be really valuable for the clarity of the $\mathbb{C}$ ODSs, later evaluated.

Once the $\Delta\phi_\omega(u,v) \in \mathbb{C}$ is properly unwrapped, a *sensitivity matrix* $\boldsymbol{s}$ is needed to finally obtain the displacement field. A *sensitivity vector* $\boldsymbol{s}_r$ can be defined as the difference between the unitary vectors of the illumination ray and the observation direction in global 3D coordinates, as in Fig. 2*d*. The use of more than 3 distinct *sensibility vectors* brings a refined *sensitivity matrix* $\boldsymbol{s}$, through a more robust (in a least-squares sense) pseudo-inversion. Therefore, from a pair of unitary vectors defining the *sensitivity vector* $\boldsymbol{s}_r$ only the projection of the displacement field $\boldsymbol{d}_\omega(u,v) \in \mathbb{C}$ along $\boldsymbol{s}_r$ can be obtained, with the following relation:

$$\Delta\phi_{\omega_r}(u,v) = (2\pi/\lambda_L)\boldsymbol{d}_\omega(u,v) \cdot \boldsymbol{s}_r \in \mathbb{C}, \tag{6}$$

stating the relation of one $\lambda_L$ (wavelength of the coherent laser light, e.g. 532 nm for a continuous wave laser as in TEFFMA project) every $2\pi$ in the *wrapped phase map* or *fringe* step, before the projection. An example is reported in Figs. 3*d*, *e*.

Instead, with a fully populated *sensitivity matrix* $\boldsymbol{s}$, the displacement field $\boldsymbol{d}_\omega(u,v) \in \mathbb{C}$ can be described in all the 3D components (being $z$ the out-of-plane direction), as:

$$\begin{bmatrix} \boldsymbol{d}_{\omega_x}(u,v) \\ \boldsymbol{d}_{\omega_y}(u,v) \\ \boldsymbol{d}_{\omega_z}(u,v) \end{bmatrix} = \frac{\lambda_L}{2\pi} \begin{bmatrix} s_{1x} & s_{1y} & s_{1z} \\ s_{2x} & s_{2y} & s_{2z} \\ s_{3x} & s_{3y} & s_{3z} \end{bmatrix}^{-1} \cdot \begin{bmatrix} \Delta\phi_{\omega_x}(u,v) \\ \Delta\phi_{\omega_y}(u,v) \\ \Delta\phi_{\omega_z}(u,v) \end{bmatrix}, \quad \boldsymbol{d}_\omega(u,v) = \frac{\lambda_L}{2\pi}\left[\boldsymbol{s}_1, \boldsymbol{s}_2, \boldsymbol{s}_3\right]^{-T} \cdot \boldsymbol{\Delta\phi}_\omega(u,v) \in \mathbb{C}. \tag{7}$$

The 3D displacement map in sensor coordinates (u,v) from Eq. (7) is later interpolated and scaled on the selected grid of measurement dofs with 3D global coordinates, with potentially contouring description.

An Ettemeyer Q500 $\mathbb{C}$-ready prototype – as shown in Figs. 2*c*, *d* with its multi(4)-illumination arms and mirrors, controlled

[17] Time averaging techniques (e.g. in Wong and Chan (1998)) are used for a fast glimpse of the average ODS with low power lighting and simple systems, but no control is left on the $\mathbb{C}$ nature of the structural dynamics. This reflects the distinction between standing and travelling ODSs, time averaging being able to acquire only standing ODSs, as can be enough in the fast assessment of musical instruments, like in the next examples, proposed for a more comprehensive reading, but not relevant for this $\mathbb{C}$-based paper: Laser-Based Interferometric Techniques for the Study of Musical Instruments, Electronic speckle pattern interferometry: Applications to the musical acoustics of percussion instruments, and An Integrated Method for the Vibroacoustic Evaluation of a Carbon Fiber Bouzouki. Instead, for travelling ODSs and generally in EFFMA, which are inherently $\mathbb{C}$, stroboscopic ESPI is compulsory to avoid any misunderstanding, with the $\mathbb{C}$ approach here summarised.

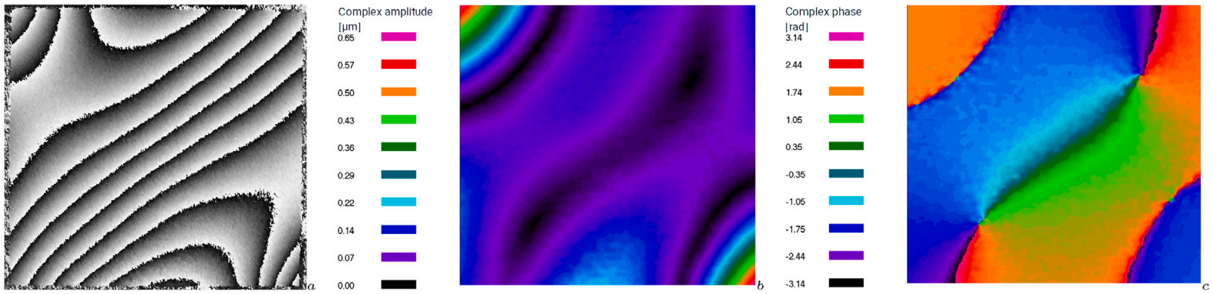


**Fig. 4.** Example of ESPI measurements at 80 Hz: in *a* the wrapped phase map from Eq. (4), in *b* the *complex amplitude* and in *c* the *complex phase*, both obtained from Eq. (5) by $K = 12$ equally phase delayed maps as in *a*.

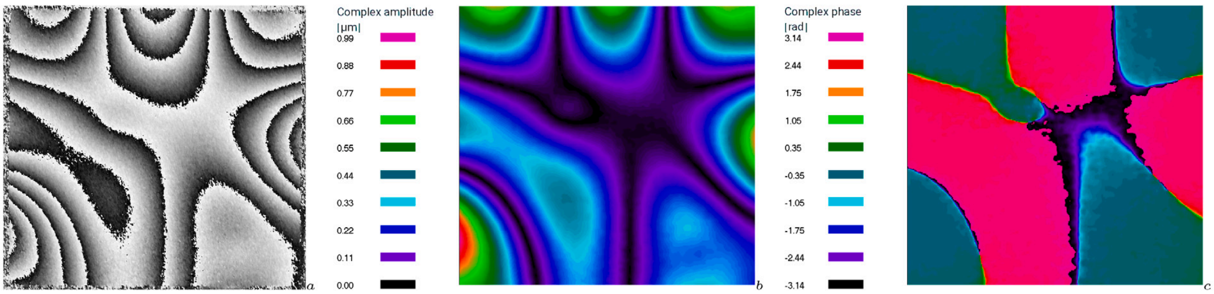


**Fig. 5.** Example of ESPI measurements at 565 Hz: in *a* the wrapped phase map from Eq. (4), in *b* the *complex amplitude* and in *c* the *complex phase*, both obtained from Eq. (5) by $K = 12$ equally phase delayed maps as in *a*.

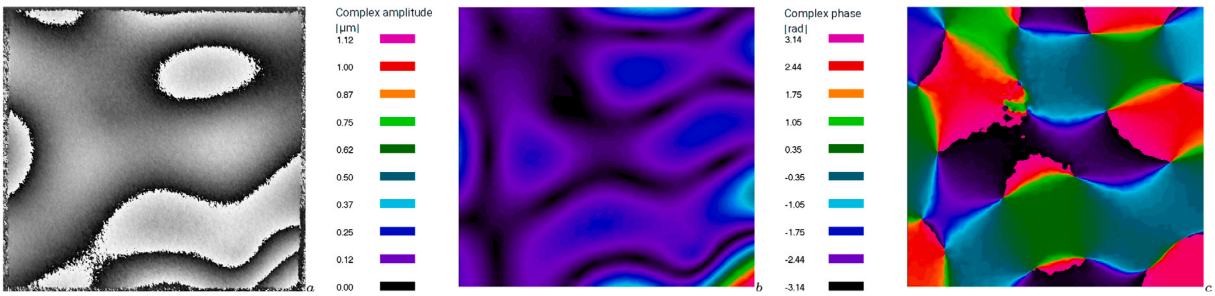


**Fig. 6.** Example of ESPI measurements at 996 Hz: in *a* the wrapped phase map from Eq. (4), in *b* the *complex amplitude* and in *c* the *complex phase*, both obtained from Eq. (5) by $K = 12$ equally phase delayed maps as in *a*.

by piezoelectric transducers for the 3D *sensitivity matrix* $s$ and phase shifting approaches (Maas, 1991; Vrooman, 1991; Schreiber and Bruning, 2007) – was used in the TEFFMA project with a high-resolution (1.3 MPixels) sensor, but limited to a 250 × 250 interpolation dofs' matrix due to the huge dataset recorded in $N = 10$ repetitions, although higher density (e.g. the standard parameter sets a 600 × 600 dofs matrix) was freely achievable in the final interpolation. In Figs. 4, 5, 6 examples of the whole stroboscopic $\mathbb{C}$ ESPI displacement maps evaluation are proposed, as taken directly out of the proprietary software Istra 3.4.2 respectively at the frequencies of 80, 565 and 996 Hz, which are close – but still different – to those later used in the *receptances*' dataset in Sections 2.2 and 5. The difference in frequency, in such a populated structural dynamics, might be enough to change the patterns. Note that only one repetition is here proposed, whereas $K = 12$ equally phase delayed maps are used to compute the virtual $\mathbb{C}$ field. The estimations in Section 2.2 are therefore made in the frequency domain by stepped sine excitation, dealing with $N \times K = 120$ unwrapped phase maps at each frequency line. Furthermore, these data were originally sampled every 0.5 Hz, whereas in Sections 2.2 and 5 an interpolation was made over the SLDV-based frequency spacing, as detailed below. In Figs. 4–6, first a $\mathbb{R}$ *wrapped phase map* is shown, as one of the many that can be obtained, with quite different patterns by changing the illumination phasing regarding the excitation from Eq. (4). Also, when *unwrapped*, such phase map should not be confused with any part of the virtual $\mathbb{C}$ field, obtained from Eq. (5) by $K$ maps of the type in Eq. (4), and shown instead in its *complex amplitude* in tiles $b$ and in its *complex phase* in tiles $c$. Specifically, the latter can show the degree of *complexity* of the $\mathbb{C}$ map, with smooth transitions of the colours in the range $[-\pi, \pi]$, and related to an increase of the relative thickness of the cloud of the map on the aforementioned *complex plane*; instead, a strictly $\mathbb{R}$ map shows always sharp changes of *complex phase* sign, to the opposite extremes, with all the dofs-related segments laying on the same straight line.

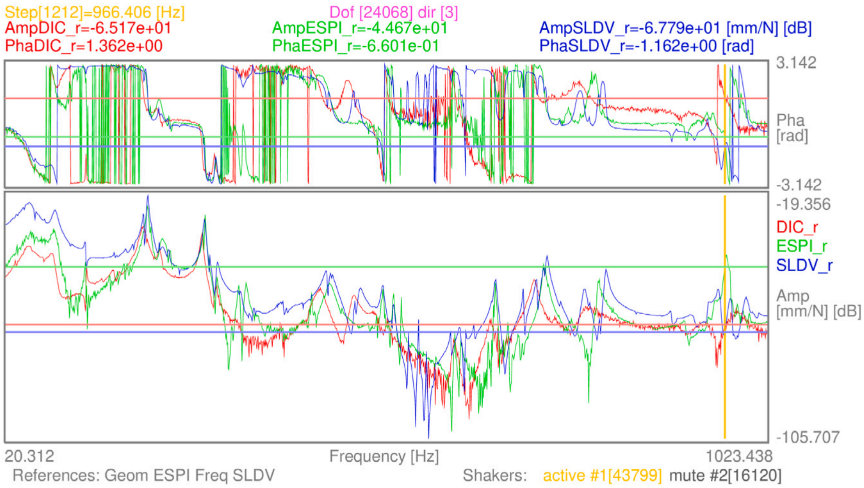


**Fig. 7.** Example of *receptance* $\boldsymbol{H}_{\boldsymbol{d}_{qS_1}}(\omega)$ graph in the frequency domain evaluated in structural dof $q = 24068$ – by means of DIC (red), ESPI (green) and SLDV (blue) techniques from the TEFFMA project – with shaker 1 excitation.

To achieve the *dense* detail in the full-field *receptances*, the ESPI-based results are here used as geometry reference in the topology transforms at their *native* resolution, with nearly 1 dof every linear mm in a 240 × 226 mm map – about 5 mm inside the borders of the plate, which brought 226 × 217 (49042) structural dofs. SLDV and DIC, as in footnote 16 and in Zanarini (2018, 2019a,b), could not reach such density and field-wise quality[18] on the same rig, recalling from above how ESPI was restrained in the number of dofs. ESPI-based *receptances* are here instead interpolated in the frequency domain onto the SLDV-based frequency granularity, thus resulting in 1285 – instead of the over 2000 acquired ones – frequency lines in the range [20–1024] Hz, with 0.78125 Hz of even frequency spacing, remaining more manageable for the scopes of this paper.

### 2.2. Brief recall of a direct full-field FRF characterisation

The well known formulation of *receptance* matrix $\boldsymbol{H}_{\boldsymbol{d}_{qf}}(\omega)$, as spectral linear relation between *displacements* and *forces* under the assumption of noise only in the output ($H_1$ estimator (Ewins, 2000; Heylen et al., 1998; Bendat and Piersol, 2000)), will here be used for the *full-field FRF* estimation. $\boldsymbol{H}_{\boldsymbol{d}_{qf}}(\omega)$ describes the dynamic behaviour of a linearised – for its geometrical configuration and its material properties at the specific dynamic conditions – testing system, with potentially $N_f$ input excitations $\boldsymbol{F}_{\boldsymbol{f}}(\omega) = [\boldsymbol{F}^T_{f_1}(\omega) \dots \boldsymbol{F}^T_{f_{N_f}}(\omega)]^T$ in structural locations of global coordinates $\boldsymbol{q}_{\boldsymbol{f}} = [\boldsymbol{q}^T_{f_1} \dots \boldsymbol{q}^T_{f_{N_f}}]^T$ (with $\boldsymbol{q}_{\boldsymbol{f}}$ being the global coordinates of all the input forces' locations, here 2 distinct shakers) and $N_q$ output displacement responses $\boldsymbol{X}_{\boldsymbol{q}}(\omega) = [\boldsymbol{X}^T_{q_1}(\omega) \dots \boldsymbol{X}^T_{q_{N_q}}(\omega)]^T$ in structural locations of global coordinates $\boldsymbol{q}_{\boldsymbol{q}} = [\boldsymbol{q}^T_{q_1} \dots \boldsymbol{q}^T_{q_{N_q}}]^T$ ($\boldsymbol{q}_{\boldsymbol{q}}$ representing the configuration of the undeformed structure in its $N_q$ dofs, here indeed several thousands of them covering the whole sensed surface). $\boldsymbol{H}_{\boldsymbol{d}_{qf}}(\omega)$ can be formulated in the following expression for the generic single input force $f$ and output displacement $q$, as:

$$\boldsymbol{H}_{\boldsymbol{d}_{qf}}(\omega) = \frac{\sum_{m=1}^{N} S^m_{\boldsymbol{X}_q \boldsymbol{F}_f}(\omega)}{\sum_{m=1}^{N} S^m_{\boldsymbol{F}_f \boldsymbol{F}_f}(\omega)} \in \mathbb{C}, \tag{8}$$

[18] For the SLDV system in use in the TEFFMA project as in Section 2.1, scanning-related issues – in precisely driving the piezoelectric-actuated mirrors for long-lasting acquisitions – were supposed to be the main restraints in achieving higher densities. Furthermore, the noise in the spatial fields was relevantly higher than with the *native* full-field techniques, as can be seen in Zanarini (2019a,b, 2020) and in EFFMA-related or model updating results. Indeed, most of the times, the SLDV measurements are treated by a spatial smoothing (e.g. mean, median) filter in standard applications, not applied instead in the TEFFMA project's works for comparisons of raw outputs and not to lose spatial details. The effects of the scanning-related issues, as added to the more uniform random noise at some specific frequency lines, can be clearly seen in Zanarini (2020, 2023b) as specific noise patterns on the *receptances*, with a propagation into the acoustic pressure fields of Zanarini (2023b). When spatially derived, as in Zanarini (2022a, 2025), the ODSs affected by the scanning-related issues brought less reliable full-field rotational, strain and stress FRF maps. The interested reader may find different scanning-related patterns with other instrumentations, although this problem was revealed only by an accurate post-processing and not by the system's checks on raw data acquisition, as noted in Zanarini (2018, 2019a,b); this problem brought to the rejection of many SLDV datasets, with stronger faults than those later processed. For the DIC system in the TEFFMA project's works, the electronics characteristics of the cameras – set as a trade-off between possible image resolutions and frame rates – were the limit for higher spatial densities (see Zanarini (2018, 2019a,b, 2024b,c)).

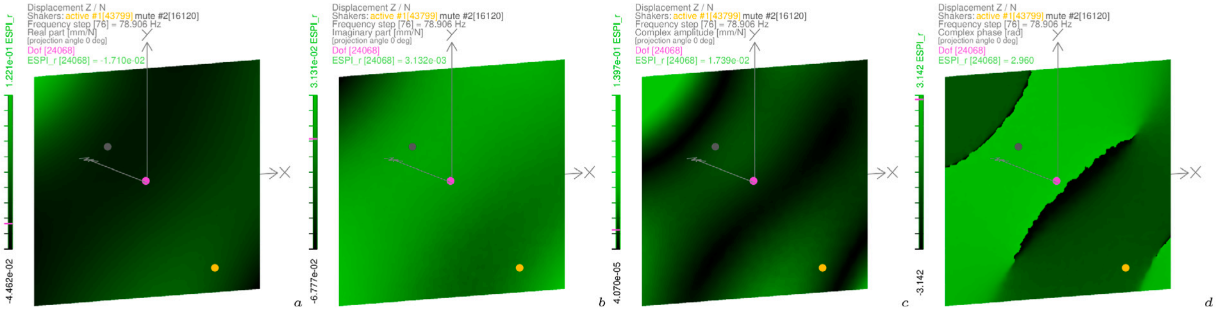


**Fig. 8.** Examples of *receptance* $\boldsymbol{H}_{d_{nqS_1}}(\omega)$ ODS evaluated at the specific frequency of 78.9 Hz, highlighted (magenta) structural dof $q$ = 24068, in its parts: *real part* in $a$, *imaginary part* in $b$, *complex amplitude* in $c$ and *complex phase* in $d$.

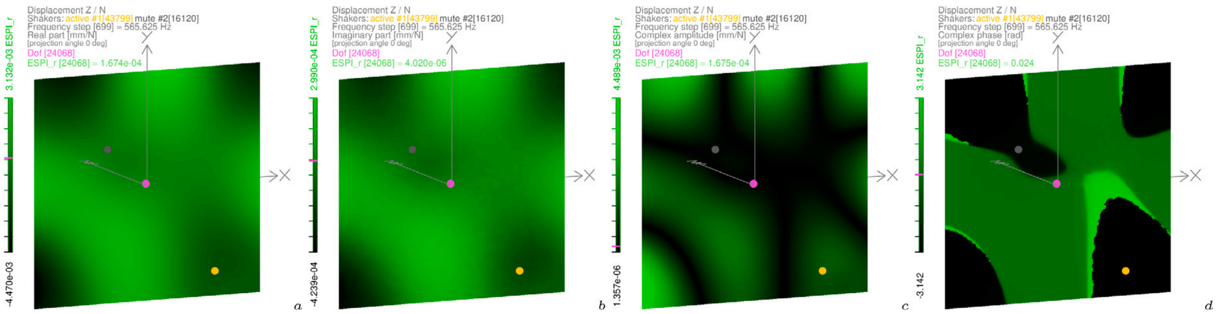


**Fig. 9.** Examples of *receptance* $\boldsymbol{H}_{d_{nqS_1}}(\omega)$ ODS evaluated at the specific frequency of 565.62 Hz, highlighted (magenta) structural dof $q$ = 24068, in its parts: *real part* in $a$, *imaginary part* in $b$, *complex amplitude* in $c$ and *complex phase* in $d$.

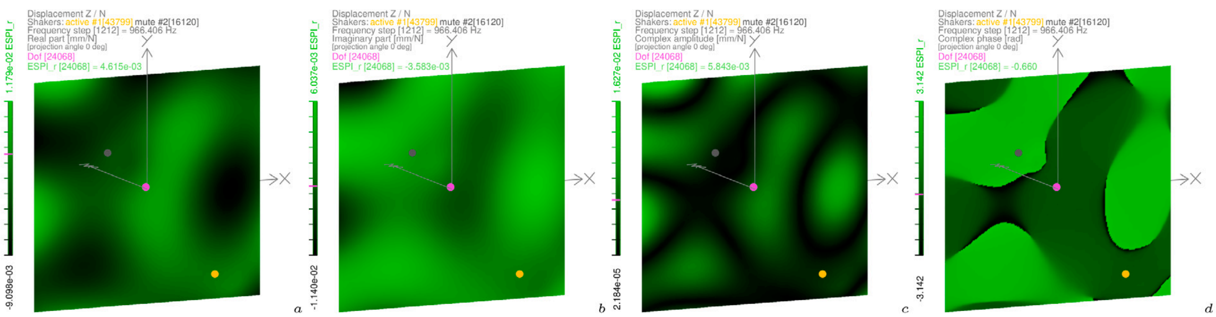


**Fig. 10.** Examples of *receptance* $\boldsymbol{H}_{d_{nqS_1}}(\omega)$ ODS evaluated at the specific frequency of 996.41 Hz, highlighted (magenta) structural dof $q$ = 24068, in its parts: *real part* in $a$, *imaginary part* in $b$, *complex amplitude* in $c$ and *complex phase* in $d$.

where $\boldsymbol{X}_q \in \mathbb{C}$ is the 3D output displacement at $q$-th structural dof located in the global coordinate $\boldsymbol{q}_q \in \boldsymbol{q}_q$, induced by the input force $\boldsymbol{F}_f \in \mathbb{C}$ at $f$-th structural dof in the global coordinate $\boldsymbol{q}_f \in \boldsymbol{q}_f$, while $S^m_{\boldsymbol{X}_q \boldsymbol{F}_f}(\omega)$ is the $m$th cross-power spectral density between input and output, $S^m_{\boldsymbol{F}_f \boldsymbol{F}_f}(\omega)$ is the $m$th auto-power spectral density of the input, evaluated in $N$ repetitions, $N$ = 10 as remarked in Section 2.1.1. Note that, although each of the ESPI-based fields is already of great quality, the noise in Eq. (8) is remarkably limited (see also the very field-wise clean *Coherence functions* in Zanarini (2018, 2019a)), thanks to the $N$ repetitions, processing $N \times K$ = 120 unwrapped phase maps at each frequency line.

A clear example of Eq. (8) can be seen in Fig. 7, where all the 3 measurement technologies (DIC in red, ESPI in green, SLDV in blue) of the TEFFMA project gave their estimation of the *receptance FRF* $\boldsymbol{H}_{d_{qf}}(\omega)$ (for the out-of-plane Z component signalled by "dir [3]", with logarithmic complex amplitude of [mm/N] in the same scale). Thanks to the topology transforms, the *receptances* are taken in the same structural dof of enquiry, here dof $q$ = 24068, close to the centre of the plate, as later shown in Figs. 8, 9 and 10 with a magenta dot; the excitation is from shaker 1 in the structural dof $f = f_1 = 43799 = S_1$. The topology transforms for all the 3 techniques used ESPI for the geometry reference and SLDV for the frequency reference, as highlighted at the bottom left of Fig. 7. No smoothing was applied to the any *receptance*.

Instead, in Fig. 8 the entire *receptance* ODS – highlighted as "Displacement Z/N" – at 78.9 Hz is displayed in its data parts with related quantities – all deployed with the same projection angle to keep consistency in the comparisons – by means of green tones of increasing brightness, from the minimal to the maximal value. The bar on the left side depicts the entire range in the single ODS, with a magenta line corresponding to the ODS value reached in the dof of enquiry, also recalled by the green text. In the tiles of Figs. 8–10, also the shakers' positions are highlighted, with a dark yellow dot for the active shaker (here shaker 1), and a grey dot for the mute one (here shaker 2, in structural dof $f = f_2 = 16120 = S_2$). A grey axes triad is partially visible, specifically showing the out-of-plane $Z$-axis orientation. Other ODS are shown in Figs. 9 and 10, at 565.62 Hz and 996.41 Hz respectively, as these 3 ODSs are later used in the vibro-acoustic simulations: in this way, the shape of the air-pumping vibrating surface is clear.

Once – as later developed in Section 4 – the specific *excitation signature* $\boldsymbol{F}_f(\omega)$ in structural dof $f$ is known in the frequency domain, the *FRF* formulation in Eq. (8) can be used to obtain the full-field *displacements* over the entire surface, as follows, at specific output dof $q$:

$$\boldsymbol{d}_{qf}(\omega) = \boldsymbol{H}_{\boldsymbol{d}_{qf}}(\omega)\boldsymbol{F}_f(\omega) \in \mathbb{C}, \tag{9}$$

The surface *velocity* in dof $q$, due to the excitation $\boldsymbol{F}_f(\omega)$, easily comes, $i$ being the imaginary unit, as:

$$\boldsymbol{v}_{qf}(\omega) = i\omega\boldsymbol{d}_{qf}(\omega) = i\omega\boldsymbol{H}_{\boldsymbol{d}_{qf}}(\omega)\boldsymbol{F}_f(\omega) \in \mathbb{C}. \tag{10}$$

Increasing the spatial resolution in hybrid models by means of *dense* full-field *FRFs* is therefore a valuable addition to the state-of-the-art of the design of complex systems and surely leads to the exploration of new FRF-based quantities derived from excellent quality displacement fields, such as surface rotations, velocities, strains & stresses and failure point distributions (Zanarini, 2018, 2019b, 2022a). Furthermore, distributed loading patterns, such as those resulting from vibro-acoustics (Zanarini, 2022c, 2023a,b, 2024a), might be considered.

## 3. Methods: revisiting a simple sound pressure vibro-acoustic formulation

To highlight what can be achieved in vibro-acoustics by ESPI *dense* experiment-based full-field *receptances*, the basic vibro-acoustic approach of the Rayleigh integral approximation is here revisited, starting from the traces found in Maynard et al. (1985), Veronesi and Maynard (1987), Williams (1999), Kirkup (1994), Gérard et al. (2002), Fahy (2003), Desmet (2004), Wind et al. (2006), Kirkup and Thompson (2007), Arenas (2008), Richards et al. (2018), Kirkup (2019), Conta et al. (2020), but without any further discussion on other methodologies, outside the scope of this paper. Pivotal is the aid of the *dense* experiment-based full-field *receptances* from ESPI, instead of any other numerical model of the structure (e.g. finite or boundary elements (Kirkup, 1994; Desmet, 2004; Kirkup and Thompson, 2007; Kirkup, 2019), wave-based (Desmet, 1998; van Hal et al., 2005; Deckers et al., 2014) or any functional expansion), and of $\mathbb{C}$ excitation signals. As hinted in Section 2.1, the construction of the set-up permits the use of the Rayleigh approach – for semi-infinite spaces – instead of the complete solution of the Helmholtz equation – for infinite spaces – thanks to the practically absent reflections of sound waves by close surfaces.

The vibro-acoustic simulation here discussed concerns the sound radiated to a theoretically infinite acoustic domain by a finite vibrating surface S, mounted on an infinite baffle to avoid any other uncontrolled source or reflection, i.e., the flat plate whose structural dynamics was here measured, as explained in Section 2.1, positioned away from reflecting surfaces, as can be seen in Fig. 2*a*. The case is that of propagating waves (Mas and Sas, 2004) in an infinite medium, revisited with a full-field *receptances*-based frequency domain approach. The *sound pressure* $p(a,\omega)$ – in the $a$th point of global coordinates $\boldsymbol{a}_a$ of the acoustic domain $A$ – can be defined, according to Kirkup (1994), Desmet (2004), Wind et al. (2006), Kirkup and Thompson (2007), Richards et al. (2018), Kirkup (2019), Conta et al. (2020), from the Rayleigh integral of the Helmholtz equation as:

$$p(a,\omega) = 2i\omega\rho_0 \int_S v_n(q,\omega)G(r_{aq},\omega)dS_q, \qquad G(r_{aq},\omega) = \frac{e^{-ikr_{aq}}}{4\pi r_{aq}} = \frac{e^{-i\omega r_{aq}/c_0}}{4\pi r_{aq}} \in \mathbb{C}, \tag{11}$$

where $\rho_0$ is the medium (air) density, $v_n(q,\omega)$ is the normal (out-of-plane) velocity of the $q$th structural centroid (located in the global coordinate $\boldsymbol{q}_q$) of the infinitesimal vibrating surface $dS_q$, $k = \omega/c_0 = 2\pi/\lambda_a$ is the wavenumber in the Helmholtz equation ($c_0$ is the speed of sound at rest in the medium, $\lambda_a$ is the acoustic wavelength), $r_{aq} = \|\boldsymbol{r}_{aq}\|$ is the norm of the distance $\boldsymbol{r}_{aq} = \boldsymbol{a}_a - \boldsymbol{q}_q$ between the specific points $(a,q)$ in the two domains, and $G(r_{aq},\omega)$ is the free space Green function as described in Eq. (11).

The normal velocities in the frequency domain can be linked to the dynamic out-of-plane displacements superposition over the static configuration $\boldsymbol{q}_q$, by means of the projection of the Eqs. (9) and (10) towards the surface normal $\hat{\boldsymbol{z}}$. Taking only the normal component of the 3D vectorial quantities, the relation $v_n(q,\omega) = \hat{\boldsymbol{z}} \cdot \boldsymbol{v}_q(\omega) = i\omega\hat{\boldsymbol{z}} \cdot \boldsymbol{d}_q(\omega) = i\omega\boldsymbol{d}_{nq}(\omega)$ can be seen as expressions of $\boldsymbol{d}_{nq}(\omega) = \boldsymbol{H}_{\boldsymbol{d}_{nqf}}(\omega) \cdot \boldsymbol{F}_{\boldsymbol{f}}(\omega)$, where the *receptance FRFs* $\boldsymbol{H}_{\boldsymbol{d}_n}(\omega) = \hat{\boldsymbol{z}} \cdot \boldsymbol{H}_{\boldsymbol{d}}(\omega)$ are of size $N_q \times N_f$, $N_q$ being the number of the structural outputs on surface S and $N_f$ of the input *excitation signatures* $\boldsymbol{F}_{\boldsymbol{f}}(\omega)$. Eq. (11) can be therefore rewritten as:

$$p(a,\omega) = -2\omega^2\rho_0 \int_S \boldsymbol{H}_{\boldsymbol{d}_{nqf}}(\omega)\boldsymbol{F}_{\boldsymbol{f}}(\omega)G(r_{aq},\omega)dS_q \in \mathbb{C}, \tag{12}$$

with $\boldsymbol{H}_{\boldsymbol{d}_{nqf}}(\omega)$, $\boldsymbol{F}_{\boldsymbol{f}}(\omega)$ and $G(r_{aq},\omega)$ as $\mathbb{C}$ quantities, therefore also the field $\boldsymbol{p}(\boldsymbol{a},\omega) \in \mathbb{C}$.

By means of a discretisation of the vibrating surface domain $S$ that scatters the sound pressure, like $S \approx \sum_q \Delta S_q$, where $\Delta S_q$ is the discrete rectangular area of the surface with the $q$th point as centroid and dimensions as an average of the distances from the neighbour points in the grid, Eq. (12) can be expressed in terms of a sum of discrete contributions, as a full-field *receptances*-based Rayleigh integral approximation:

$$p(a,\omega) \approx -2\omega^2\rho_0 \sum_{q}^{N_q} \boldsymbol{H}_{\boldsymbol{d}_{nqf}}(\omega)\boldsymbol{F}_{\boldsymbol{f}}(\omega)G(r_{aq},\omega)\Delta S_q \in \mathbb{C}, \tag{13}$$

with $\boldsymbol{H}_{\boldsymbol{d}_{nqf}}(\omega)$, $\boldsymbol{F}_{\boldsymbol{f}}(\omega)$ and $G(r_{aq},\omega)$ now related to discrete domains, with $\boldsymbol{a}_{\boldsymbol{a}} = [\boldsymbol{a}_{a_1}^T \dots \boldsymbol{a}_{a_{N_a}}^T]^T$ being the global 3D coordinates of the $N_a$ dofs in the mapped acoustic domain.

Being $G(r_{aq},\omega)$ and $\Delta S_q$ functions of the locations of the $N_a$ discrete points in the whole acoustic domain and of the $N_q$ points on the vibrating surface, they can be grouped in a *diffusion matrix* $\boldsymbol{T}_{\boldsymbol{aq}}(\omega) \in \mathbb{C}$, sized $N_a \times N_q$, of single element $\boldsymbol{T}_{aq}(\omega) = -2\omega^2\rho_0 G(r_{aq},\omega)\Delta S_q$, to transform the summation of Eq. (13) into a matrices' product for the *acoustic pressure* in the single point $a$:

$$p(a,\omega) \approx \boldsymbol{T}_{\boldsymbol{aq}}(\omega)\boldsymbol{H}_{\boldsymbol{d}_{nqf}}(\omega)\boldsymbol{F}_{\boldsymbol{f}}(\omega) \in \mathbb{C}. \tag{14}$$

If, differently than the *acoustic transfer vectors* in Gérard et al. (2002), Citarella et al. (2007) as functions between *acoustic pressures* and *surface velocities*, a *vibro-acoustic transfer matrix* $\boldsymbol{V}_{\boldsymbol{af}}(\omega)$, sized $N_a \times N_f$, is defined as:

$$\boldsymbol{V}_{\boldsymbol{af}}(\omega) = \boldsymbol{T}_{\boldsymbol{aq}}(\omega) \cdot \boldsymbol{H}_{\boldsymbol{d}_{nqf}}(\omega) \in \mathbb{C}, \tag{15}$$

therefore as a functional of *acoustic pressures* over *structural forces* containing the structural dynamics of the radiating surface, Eq. (14) can be easily rewritten as:

$$p(a,\omega) \approx \boldsymbol{V}_{af}(\omega)\boldsymbol{F}_{\boldsymbol{f}}(\omega) \in \mathbb{C}, \tag{16}$$

which turns useful if the structural responses and acoustic domain are kept unchanged (meaning the *vibro-acoustic transfer matrix* $\boldsymbol{V}_{\boldsymbol{af}}(\omega)$ is unchanged), while varying only the excitation signatures to map the responses on the *acoustic pressure* field $\boldsymbol{p}(\boldsymbol{a},\omega)$.

The *diffusion matrix* $\boldsymbol{T}_{\boldsymbol{aq}}(\omega)$ allows the estimation of the *pressure* field by means of matrix multiplications, which are made just bigger in the case of finer grids in both the acoustic and structural domains. While working on a quantitative comparison of the results from reduced datasets of the 3 full-field optical measurement techniques in the TEFFMA project, the tentative parallelisation – mentioned for (Zanarini, 2022c, 2023a,b) – was applied on the *diffusion matrix* $\boldsymbol{T}_{\boldsymbol{aq}}(\omega)$, shared in the 3 simulations, the structural and acoustic domains being the same among the experiment-based approaches, therefore worthy for a single shared memory allocation and calculation, but within the computational constraints of physical memory.

Note also that Eqs. (14) and (16) allow the calculation of the *sound pressure* field directly from experiment-based full-field *receptances*, which should help the accuracy of the *dense* results in all their $\mathbb{C}$ parts. One should be aware that other researchers, also focused on other simulation methods not of concern here, work with *sound powers* in much coarser grids – losing all precise *phase* information – and are therefore of no specific interest in this discussion that instead stresses the $\mathbb{C}$ nature of the experiment-based quantities in *dense* domains. The results proposed in Section 5 can be achieved thanks to the extreme spatial density and accuracy of the *dense* ESPI full-field *receptances*, and because these *receptances* – being evaluated directly from the test – retain the true blending of any $\mathbb{C}$ ODS active at the specific frequency, with the proper real boundaries and dissipation/damping effects of the actual vibrating structure.

### 3.1. Comments on the approximations in the full-field receptances-based Rayleigh approach

Usually $\boldsymbol{r}_{aq}$s in Eqs. (11)–(13) are considered as constant and $\mathbb{R}$ vectors, depending only on the static locations of the points in both acoustic and structural domains. It might be noted, instead, that $\boldsymbol{r}_{aq}$ may become $\hat{\boldsymbol{r}}_{aq}(\omega) = \boldsymbol{a}_a - \boldsymbol{q}_q - \boldsymbol{H}_{\boldsymbol{d}_{nqf}}(\omega) \cdot \boldsymbol{F}_{\boldsymbol{f}}(\omega) \in \mathbb{C}$, once the structural domain is considered in small-amplitude flexible motion, dependent on excitation, structural dynamics and frequency. Nonetheless, being the contributions $\boldsymbol{H}_{\boldsymbol{d}_{nqf}}(\omega) \cdot \boldsymbol{F}_{\boldsymbol{f}}(\omega) \in \mathbb{C}$ considered of at least 3 orders of magnitude lower than the static distances $\boldsymbol{r}_{aq}$s when far from the sound pressure source, at first evaluation they can be neglected, but might be a source of future discussion for Nearfield Acoustic Holography (NAH). The same can be said about the small variations of $\hat{\boldsymbol{z}}$, due to the surface deflection that pushes the air in a direction slightly different from the actual constant normal. Considering $\boldsymbol{r}_{aq}$s as $\mathbb{R}$ constant vectors – independent of frequency, structural dynamics and excitations – brings clear advantages in the amount and speed of calculations, thanks to a single computation and memory allocation, with potentially great advantages in parallel computing.

Also the wavenumber $k$ in Eq. (11), in some problems like those of damped waves (Fahy, 2003) or of specific medium conditions, may become *complex-valued*, such that $\hat{k}^2 = \omega(\omega + i\gamma)/c_0{}^2$ with damping parameter $\gamma > 0$, when the waves are absorbed by the medium through which they propagate. There also results, with $\hat{k}(\omega), \hat{r}_{aq}(\omega) \in \mathbb{C}$, that a more extended Green function $\hat{G}(\hat{r}_{aq}(\omega),\omega) = e^{-i\hat{k}(\omega)\hat{r}_{aq}(\omega)}/4\pi\hat{r}_{aq}(\omega)$ should have been introduced, with $e^{c(\omega)} = e^{d(\omega)+ib(\omega)} = e^{d(\omega)}(cosb(\omega) + isinb(\omega))$, $c(\omega) = -i\hat{k}(\omega)\hat{r}_{aq}(\omega) = d(\omega) + ib(\omega) \in \mathbb{C}$. But in the simplified problem of sound radiated into air – from a metal structure like the one presented here – the wavenumber $k$ is kept *real-valued* with $\gamma = 0$, as well as $\boldsymbol{r}_{aq} \in \mathbb{R}$, therefore the Green function $G(r_{aq},\omega)$ results with $e^c = e^{0+ib} = (cosb + isinb)$ as $G(r_{aq},\omega) = (cos(-kr_{aq}) + isin(-kr_{aq}))/4\pi r_{aq}$, $\Re(G(r_{aq},\omega)) = cos(-\omega r_{aq}/c_0)/4\pi r_{aq}$, $\Im(G(r_{aq},\omega)) = sin(-\omega r_{aq}/c_0)/4\pi r_{aq}$, as approximated in Eq. (11).

## 4. Methods: formulation in the frequency domain of dynamic signatures for excitation forces

In order to fully appreciate the contribution of experiment-based full-field *receptances*, thanks to their $\mathbb{C}$ representation of the real-life structural dynamics, different excitation signatures for $\boldsymbol{F}_f(\omega) = [F_{Re}(\omega), F_{Im}(\omega)]$ *real* & *imaginary* components are discussed in the following subsections. The general shape of the amplitude-modulated broad frequency band forces is here that of the coloured noises as inspired by Wikipedia.org (2025), governed by the $1/\omega^{\alpha}$ factor, with $\alpha \in [-2, 2]$ defining the *noise colour*: $\alpha = -2$ for *violet noise*, $\alpha = -1$ for *blue noise*, $\alpha = 0$ for *white noise*, $\alpha = 1$ for *pink noise* and $\alpha = 2$ for *red noise*. For all types of excitations, shared quantities can be defined: $F_0$ as the reference amplitude; $S_0$ as the sinusoidal phase range multiplier; $N_p$ as the number of half cycles of the phase in the range; $\omega_0$ as the starting frequency; $\Delta\omega$ as the frequency range; $\theta_0$ as a reference phase; $\theta(\omega) = S_0 sin(\pi N_p(\omega - \omega_0)/\Delta\omega + \theta_0)$ as a selected phase function; $\beta_{F_0}$, being $0 \leq \beta_{F_0} \leq 1$, as the level of randomness in the amplitude; $Rand_{F_0}$ and $Rand_{\theta}$ as functions returning a pseudo-random number in the range 0 to 1; $\beta_{\theta}$ as the level of randomness in the phase compared to $\pi$. For all the examples later provided in Section 5, the following inputs were taken: $F_0 = 0.050$ N, $S_0 = 1.0$ rad, $N_p = 7.5$, $\theta_0 = 0.5\pi$ rad, $\beta_{F_0} = 1.0$, $\beta_{\theta} = 3.14/\pi$.

### 4.1. Real-valued coloured noise

A $\mathbb{R}$ *coloured noise* excitation $\boldsymbol{F}(\omega)$ can be defined as:

$$F_{Re}(\omega) = \frac{F_0}{\omega^{\alpha}}, F_{Im}(\omega) = 0, \boldsymbol{F}(\omega) = \left[F_{Re}(\omega), F_{Im}(\omega)\right] \in \mathbb{C}. \tag{17}$$

This means, therefore, that each frequency line component has the same *phase*, simply put to zero *phase* lag and null *imaginary part* $F_{Im}(\omega)$. This type of noise receives here the label "*std*", which stands for *standard* designation, and corresponds to the excitation signature already found in Zanarini (2022c, 2023a, 2024a).

### 4.2. Complex-valued coloured noise

A $\mathbb{C}$ *coloured noise* excitation $\boldsymbol{F}(\omega)$ can be defined as:

$$\boldsymbol{F}(\omega) = \frac{F_0}{\omega^{\alpha}} e^{i\theta(\omega)} \in \mathbb{C}, \tag{18}$$

with $\theta(\omega)$ to address the varying *phase* with a specific function, as above. This type of noise receives here the label "*sp*", which stands for *sinusoidal phase* designation, as can be found in Figs. 24, 26, 27 and 28. It can be seen how all the complexity of the clean excitation can be described with this type of signal.

### 4.3. Real-valued coloured noise with random amplitude variations

A $\mathbb{R}$ *coloured noise* excitation *with random amplitude variations* $\boldsymbol{F}(\omega)$ can be defined as:

$$F_{Re}(\omega) = \frac{F_{0_r}}{\omega^{\alpha}}, F_{Im}(\omega) = 0, \boldsymbol{F}(\omega) = \left[F_{Re}(\omega), F_{Im}(\omega)\right] \in \mathbb{C}. \tag{19}$$

This means therefore that each frequency line component has the same *phase*, simply put to zero *phase* lag. Specifically: $F_{0_r} = F_0(1 + \beta_{F_0}(Rand_{F_0} - 0.5))$, where $F_0$ can be seen as the reference – or mean – amplitude, around which the randomness occurs. This type of noise receives here the label "*ra*", which stands for *random amplitude* – but zero *phase* lags – designation.

### 4.4. Complex-valued coloured noise with random amplitude & phase variations

A $\mathbb{C}$ *coloured noise* excitation *with random amplitude* & *phase variations* $\boldsymbol{F}(\omega)$ can be defined as:

$$\boldsymbol{F}(\omega) = \frac{F_{0_r}}{\omega^{\alpha}} e^{i\theta_r(\omega)} \in \mathbb{C}. \tag{20}$$

Specifically, $F_{0_r} = F_0(1 + \beta_{F_0}(Rand_{F_0} - 0.5))$, where again $F_0$ is the reference amplitude, around which the amplitude randomness occurs. Identically, $\theta_r(\omega) = \theta(\omega)(1+\beta_{\theta}(Rand_{\theta} - 0.5))$ with $\theta(\omega)$ as the chosen *phase* function, contaminated by random *phase* variations. This type of noise receives here the label "*rap*", which stands for *random* variations in the *amplitude* and sinusoidal *phase* designation, as can be found in Figs. 25, 29, 30 and 31.

It can be clearly seen how this latter type of signature retraces that of any experiment-based acquisition, with a generically varied spectrum and stochastically spread uncertainty in all the signal components. Therefore, in these approaches, grounded on experiment-based full-field *receptances*, any testing force can be retained with its real-life components, without assumptions nor compromises, except the respect of the linearity relation between force levels and structural responses.

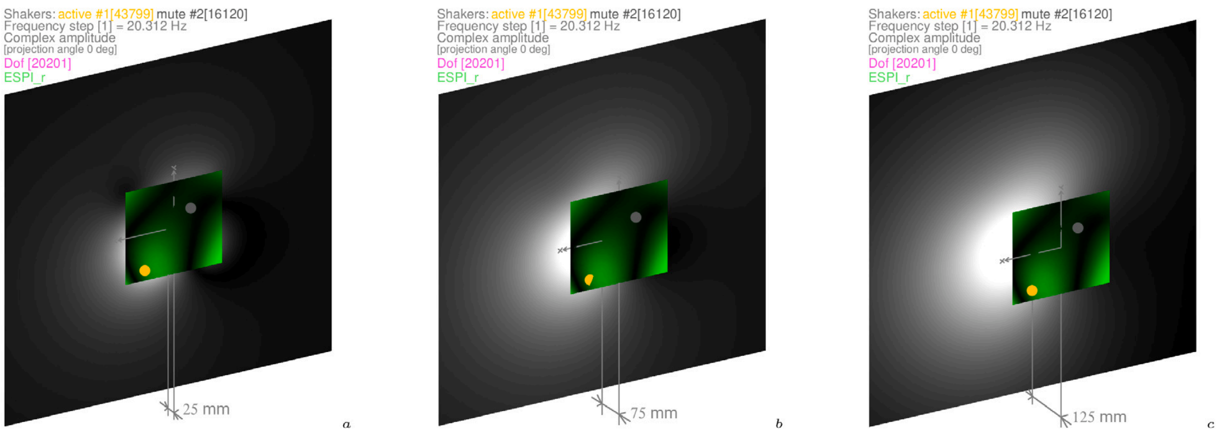


**Fig. 11.** Relative position in a reversed view of the radiating surface (in green tones) and the acoustic domain of interest (in grey tones), at specific distances of 25 mm in (*a*), of 75 mm in (*b*) and of 125 mm in (*c*), excitation from shaker 1 at 20 Hz.

## 5. Results & discussion: numerical mapping of sound pressure from full-field *receptances*

The theoretical relevance of the defined *vibro-acoustic transfer matrix* $\boldsymbol{V}_{af}(\omega)$ should be already clear, before the adoption of a specific excitation signature from Section 4, to simulate the *acoustic pressures* in Eq. (16). After brief notes on the meshing of the acoustic domain, examples of the *vibro-acoustic transfer matrix* and of the *acoustic pressure* fields are here given, with the aid of ESPI-based spatially *dense* full-field *receptances* and $\mathbb{C}$ coloured noise excitations. Brief instructions follow on how to read the text in the pictures (see Figs. 12–31) processed for showing the results of this Section.

At the first line from top of the 2D graphs, in magenta in the centre, a brief description of the main function is reported, together with the acoustic dof of enquiry, considered on the maps. At the top left, the frequency line of interest is highlighted in dark yellow, as well as the corresponding vertical line on the graphs, like a frequency cursor. Just below, the involved functions/parts (in assigned colours for each measurements technology, with pure green for ESPI) are reported with the values at the specific frequency, together with a corresponding horizontal coloured line in the frames of the graphs/parts. In all the 2D graphs, the extremes of the main function are annotated in grey text on the right side, as well as the description[19] of the quantity. When the excitation signal is introduced (in black), it is normalised to occupy only a portion of the frame of the *complex amplitude*, without extremes in evidence. However, the excitation is fully described in black at the top left of each quantity frame, together with the punctual value at the specific frequency, but without any horizontal black line. At the bottom of the graphs, below the line for the extremes of the frequency range, the geometry and frequency references of the dataset are reported in grey text on the left side, whereas the active (yellow) and mute (dark grey) shakers are indicated on the right side.

For the 3D maps, in the first text line from the top a brief description of the main function is proposed. The second text line underlines which shaker is active (in dark yellow) and mute (in dark grey), with corresponding structural dofs, possibly focused on the map by coloured dots (if the face culling allows their rendering); for these *dense* ESPI-based datasets, shaker 1 is in structural dof 43799, while shaker 2 in dof 16120. The third text line contains the frequency step and the corresponding value in Hertz. The same geometrical view and phasing angle are kept among the tiles of the $\mathbb{C}$ maps, when proper comparisons are of interest: the fourth text line reports which $\mathbb{C}$ part is figured, while the fifth line gives the specific projecting phase angle. The sixth text line, in magenta, highlights the specific dof of enquiry, also represented by a big magenta dot on the map. The seventh text line reports in pure green the numerical value of the function reached in the enquiry dof, when using ESPI-based datasets. The same value is highlighted by a magenta dash in the ranges' bar, as detailed below. The acoustic mesh is graded by grey tones, linearly ranging from pure white (rgb=[1,1,1]) in the maximum value to pure black (rgb=[0,0,0]) in the minimal value. The ranges of each specific map are reported on the left side of the tile, with the linearly varying grey tones and the extremes (in text, the highest in pure green for ESPI) of the whole range.

### 5.1. Meshing the acoustic domain

The selection of the acoustic domain's parameters should reflect the specific application, as well as the structural dynamics should be sensed accordingly, in order to have the real behaviour of the vibro-acoustic coupled domains. However, during the TEFFMA project no specific measurements were taken about the air parameters, neither for temperature, nor for humidity nor for density. All these specific conditions affect the material properties of the components and the related structural dynamics; they also have a direct

[19] If followed by the suffix "[dB]", the operator `20*log10()` is applied to the function values.

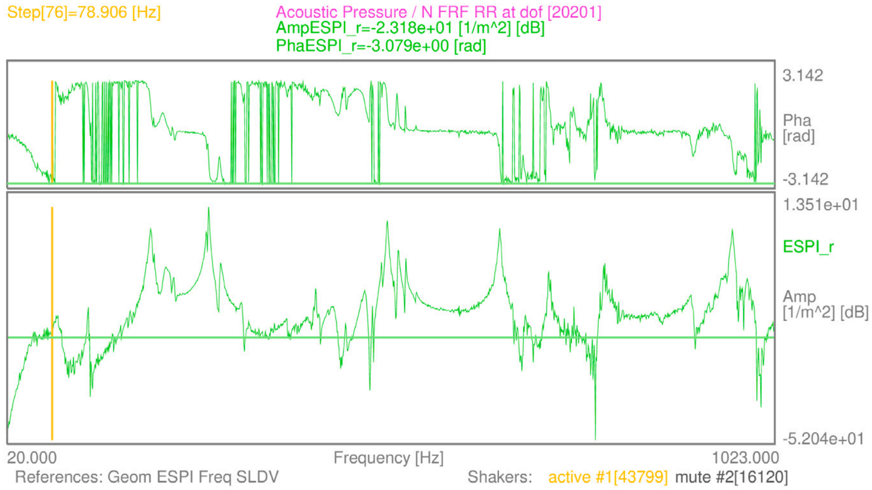


**Fig. 12.** Example of *vibro-acoustic transfer matrix* $\boldsymbol{V}_{aS_1}(\omega)$ graph in the frequency domain evaluated in acoustic dof $a$ = 20201, mesh distance of 25 mm. The frequency cursor (yellow line) intercepts the function at 78.9 Hz.

influence on the *diffusion matrix* $\boldsymbol{T}_{aq}(\omega)$, specifically by $G(r_{aq},\omega)$ and $\rho_0$; all these parameters have contributions in the *vibro-acoustic transfer matrix* $\boldsymbol{V}_{af}(\omega)$ of Eq. (15) and in the *sound pressure* fields of Eq. (16). Therefore, a generalised synthetic application – with aerospace test cases as ideal targets – is here simulated for the sake of showing the proposed approach: the air parameters for these simulations[20] were arbitrarily fixed in $c_0 = 300.0$ m/s and $\rho_0 = 1.204$ kg/m$^3$. For the aim of a simple comparison of the simulations in this paper, a squared[21] mesh was generated, of size 0.75 m × 0.75 m, with 201 × 201 dofs ($N_a$ = 40401, 3.75 mm as acoustic grid spacing). The mesh was centred on the vibrating plate and positioned at 3 increasing distances above it (0.025 m, 0.075 m, 0.125 m), as shown in Figs. 11*a*–*c*, in order to clearly appreciate the varying $\mathbb{C}$ blending effect of the pumping structural ODSs on the acoustic field. Note that, in the following figures of the acoustic mesh, the vibrating ODSs are hidden behind the mapping of the *vibro-acoustic transfer matrix* and of the *acoustic pressure* fields, the visual projection being in $-Z$ direction.

### 5.2. Evaluation of the vibro-acoustic transfer matrix

This paper wants to show the possibility of evaluating the *vibro-acoustic transfer matrix* $\boldsymbol{V}_{af}(\omega)$ directly from the experiment-based *receptances*, as proposed in Section 3, without the need of any structural FEM, but with great detail and field quality, thanks to the excellent ODSs from ESPI. It is important to underline how the *vibro-acoustic transfer matrix* obtained from the experiment-based *receptances* preserves, with its $\mathbb{C}$ nature, the real-life conditions of the test, without any simplification in the damping, nor in the materials' properties, nor in the boundary conditions, nor in any modal base identification or truncation.

In Fig. 12 a single function $\boldsymbol{V}_{af}(\omega)$ of the *vibro-acoustic transfer matrix*, evaluated with the acoustic mesh being 25 mm shifted from the vibrating plate, is reported as a frequency domain relation from shaker 1 and acoustic dof $a$ = 20201, here selected in the centre of the squared acoustic mesh. The same type of relation is reported also in Fig. 13 and in Fig. 14, at the increased distances of 75 mm and 125 mm, respectively, but, therefore, with changed patterns. The *vibro-acoustic transfer matrix* $\boldsymbol{V}_{af}(\omega)$ proved to be evaluable from full-field *receptances*, in its $\mathbb{C}$ nature highlighted in Eq. (15) and with strong interaction of the real-life structural dynamics, showing the blending of differently phased eigensystem contributions in the whole frequency range of interest. It can be clearly seen how the data retain completely the $\mathbb{C}$ nature of the experiment-based full-field *receptances*, especially in the damping around resonances and anti-resonances, or in the blending at any other frequency line. This type of results is hardly obtainable by synthetic structural models without a complete tuning or model updating. But it is also clear that, by comparing the *receptance* of Fig. 7 with the *vibro-acoustic transfer matrix* of any of the Figs. 12–14 (the acoustic dof being nearly located just above the structural dof), the *vibro-acoustic transfer matrix* $\boldsymbol{V}_{af}(\omega)$ is not a simple scaling of the *receptance* matrix $\boldsymbol{H}_{d_n}(\omega)$ of Eq. (8), but a completely new quantity, where the Green functions $G(r_{aq},\omega)$ play a relevant role in the blending of the matrix components, according to its definition. Nonetheless, the main resonance peaks of the *receptance* matrix $\boldsymbol{H}_{d_n}(\omega)$ seem to maintain a clear footprint particularly

[20] Other air parameters could be taken from Wikipedia.org (2024b) (e.g. considering a room temperature of 15 °C, close to what found, but never precisely recorded, for the TEFFMA testing: $c_0$ = 340.27 m/s and $\rho_0$ = 1.225 kg/m$^3$), but without eliminating any methodological relevance to the achievements here presented, instead with other numerical results. Further considerations must be made once the component is tested for specific in-flight conditions, the latter also affecting the material properties, therefore the whole structural dynamics. Specifically, from Wikipedia.org (2024a,b): $c_0$ drops to nearly 295–300 m/s, but the air density $\rho_0$ can vary strongly with weather conditions and with altitude in the range [1.225 (sea level) – 0.3639 (11 km) – 0.088 (20 km)] kg/m$^3$, while passing from the Troposphere (0–11 km) into the Tropopause (11–20 km), close to the cruising altitude of commercial/supersonic jets.

[21] But other meshes – manifold surfaces or point clouds included – can be easily coded for the same approach for a better appreciation of the 3D sound diffusion in other specific locations of interest.

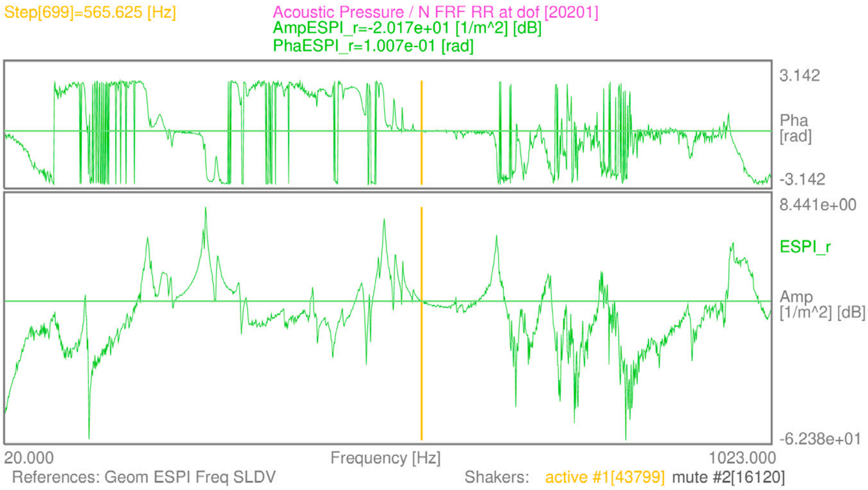


**Fig. 13.** Example of *vibro-acoustic transfer matrix* $\boldsymbol{V}_{aS_1}(\omega)$ graph in the frequency domain evaluated in acoustic dof $a = 20201$, mesh distance of 75 mm. The frequency cursor (yellow line) intercepts the function at 565.62 Hz.

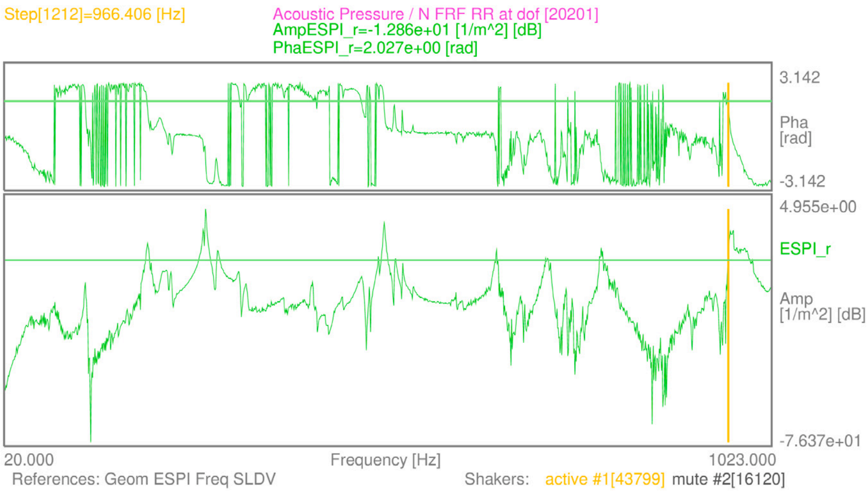


**Fig. 14.** Example of *vibro-acoustic transfer matrix* $\boldsymbol{V}_{aS_1}(\omega)$ graph in the frequency domain evaluated in acoustic dof $a = 20201$, mesh distance of 125 mm. The frequency cursor (yellow line) intercepts the function at 966.41 Hz.

in the first part of the spectra of the *vibro-acoustic transfer matrix* $\boldsymbol{V}_{\boldsymbol{af}}(\omega)$, while in the mid-high frequency range of [512–1024] Hz that influence pattern changes, with relatively higher contribution – now comparable in the *complex amplitude* – in radiating sound of other components of the *receptances*, with unexpected blending. This is partly due to the formulation of the *diffusion matrix* $\boldsymbol{T}_{\boldsymbol{aq}}(\omega)$, where $\omega^2$ multiplies the Green function (using a vector norm). Once focusing in the same mid-high frequency range, the patterns of the *vibro-acoustic transfer matrix* $\boldsymbol{V}_{\boldsymbol{af}}(\omega)$ in Figs. 12–14 seem there more affected by the distance of the acoustic mesh from the vibrating surface, again putting into evidence the blending role of the Green function $G(r_{aq}, \omega)$, which has $r_{aq}$ both in a limited numerator and in a linearly dependent denominator (see Section 3.1), $r_{aq}$s being directly affected by the distance between the domains.

In Figs. 15, 16 and 17 the *vibro-acoustic transfer matrix* $\boldsymbol{V}_{\boldsymbol{aS}_1}(\omega)$ is displayed in grey tones over the whole acoustic mesh, hiding the *receptance* matrix $\boldsymbol{H}_{\boldsymbol{d}_{nqS_1}}(\omega)$ of the radiating plate already introduced in Fig. 8 at 78.9 Hz, with the acoustic mesh at 25 mm, 75 mm and 125 mm respectively as in Fig. 11*a*–*c*, but seen from $-Z$ direction like in Fig. 8, with all the $\mathbb{C}$ components of the acoustic domain. As explained in the captions of Figs. 15–17, the *real part* is in tile *a*, the *imaginary part* is in tile *b*, the *complex amplitude* is in tile *c*, while the *complex phase* is depicted in tile *d* of each composite figure that follows. Beside each tile/component, as already introduced, the range scale in grey tones allows to locate, by means of a magenta line, the level reached by the *vibro-acoustic transfer matrix* in the acoustic dof of enquiry ($a = 20201$), which is the magenta dot highlighted in the acoustic mesh. Darker tones correspond linearly to the minimal values in the range, while full brightness pertains to the maximal values, eventually with the minus sign.

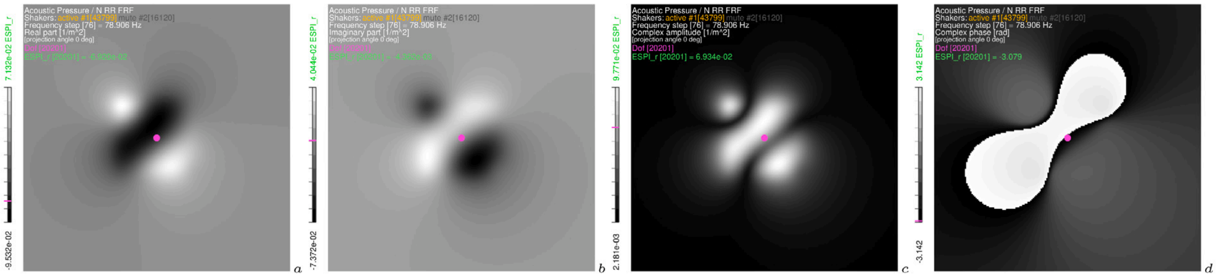


**Fig. 15.** Examples of *vibro-acoustic transfer matrix* $\boldsymbol{V}_{aS_1}(\omega)$ mesh evaluated at the specific frequency of 78.9 Hz, highlighted (magenta) acoustic dof $a = 20201$, mesh distance of 25 mm, in its parts: *real part* in $a$, *imaginary part* in $b$, *complex amplitude* in $c$ and *complex phase* in $d$.

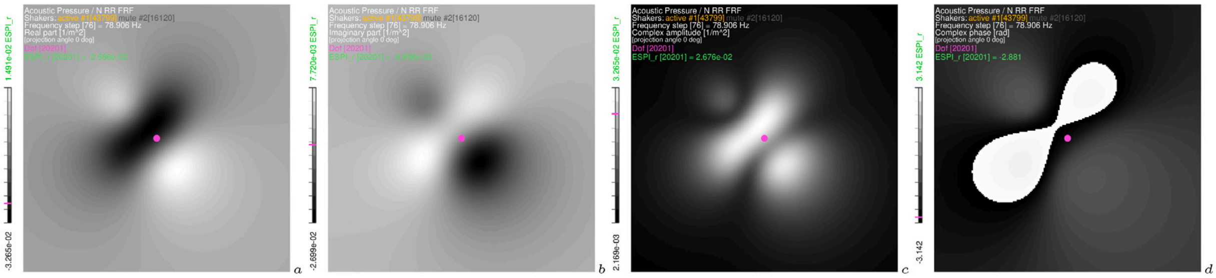


**Fig. 16.** Examples of *vibro-acoustic transfer matrix* $\boldsymbol{V}_{aS_1}(\omega)$ mesh evaluated at the specific frequency of 78.9 Hz, highlighted (magenta) acoustic dof $a = 20201$, mesh distance of 75 mm, in its parts: *real part* in $a$, *imaginary part* in $b$, *complex amplitude* in $c$ and *complex phase* in $d$.

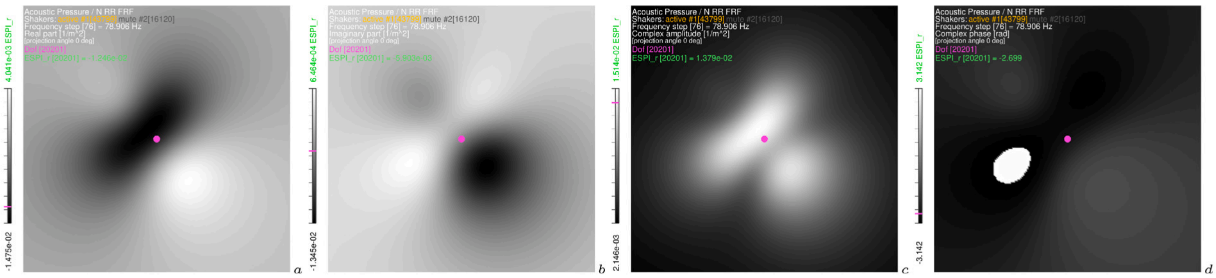


**Fig. 17.** Examples of *vibro-acoustic transfer matrix* $\boldsymbol{V}_{aS_1}(\omega)$ mesh evaluated at the specific frequency of 78.9 Hz, highlighted (magenta) acoustic dof $a = 20201$, mesh distance of 125 mm, in its parts: *real part* in $a$, *imaginary part* in $b$, *complex amplitude* in $c$ and *complex phase* in $d$.

The levels can be useful to properly understand how the components are blended, or scaled, into the whole data representation, once a specific excitation is used later to evaluate the *acoustic pressure* field of Eq. (16).

In Fig. 15$c$ the *complex amplitude* of the *vibro-acoustic transfer matrix* $\boldsymbol{V}_{aS_1}(\omega)$ is shown to exhibit a clear link to the *receptance* shape of Fig. 8$c$, as the latter is quite simple at 78.9 Hz. The agreement seems also slightly higher between the *real parts* in Fig. 15$a$ and Fig. 8$a$, rather than with the *imaginary parts* in Fig. 15$b$ and Fig. 8$b$. Instead, the *complex phase* on the *vibro-acoustic transfer matrix* in Fig. 15$d$ appears with a slightly different pattern, than the *complex phase* of the structural ODS in Fig. 8$d$, confirming the different nature of the quantities, blended by the $\mathbb{C}$ Green functions. As hinted in Section 2.1.1, the areas in the *complex phase* shapes with smoothly varying tones not belonging to the extremes $[-\pi, \pi]$ witness a high level of *complexity*, more typical of travelling waves, rather than of standing waves, which are – instead – easily represented by $\mathbb{R}$ and sharply stepped patterns. The same ODS of Fig. 8 at 78.9 Hz is the *receptance* pattern that pumps air also for the other evaluations in Figs. 16 and 17, but at increased acoustic mesh/plate distances. In the tiles of those figures, the expansion of the pattern already commented in Fig. 15 can be recognised, together with a fading, or smoothing, of the sharper profiles while the distance of the acoustic mesh from the plate increases. Except for the *complex phase* pattern (essentially raised in the wrapping by $0.198\pi$ and $0.280\pi$ rad, then brighter tones are restarted by -$2\pi$ in dark zones), the other data parts of the *vibro-acoustic transfer matrix* $\boldsymbol{V}_{aS_1}(\omega)$ are active in nearly 1/9 of the mesh at 25 mm, in 1/4–1/3 at 75 mm and in about the whole mesh at 125 mm, but still preserving resemblances to the relatively simple ODS pattern in Fig. 8, although in changing shapes thanks to the different Green functions used in the *diffusion matrix* $\boldsymbol{T}_{aq}(\omega)$ of Section 3.1.

In Figs. 18, 19 and 20 the *vibro-acoustic transfer matrix* $\boldsymbol{V}_{aS_1}(\omega)$ is displayed by the data parts in the whole acoustic mesh, but at 565.62 Hz, as generated in Eq. (15) when feeding the *receptance* ODS of Fig. 9, which has a more complex pattern than that of Fig. 8. At the close distance of 25 mm in Fig. 18, the *vibro-acoustic transfer matrix* has stronger resemblances with the *real* and *imaginary*

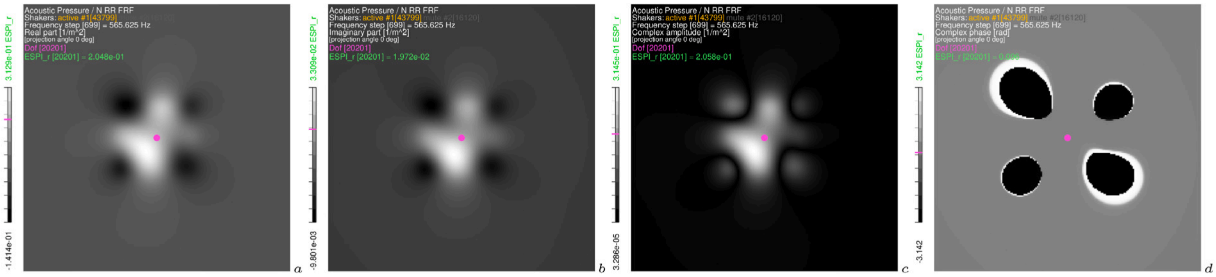

**Fig. 18.** Examples of *vibro-acoustic transfer matrix* $\boldsymbol{V}_{aS_1}(\omega)$ mesh evaluated at the specific frequency of 565.62 Hz, highlighted (magenta) acoustic dof $a = 20201$, mesh distance of 25 mm, in its parts: *real part* in $a$, *imaginary part* in $b$, *complex amplitude* in $c$ and *complex phase* in $d$.

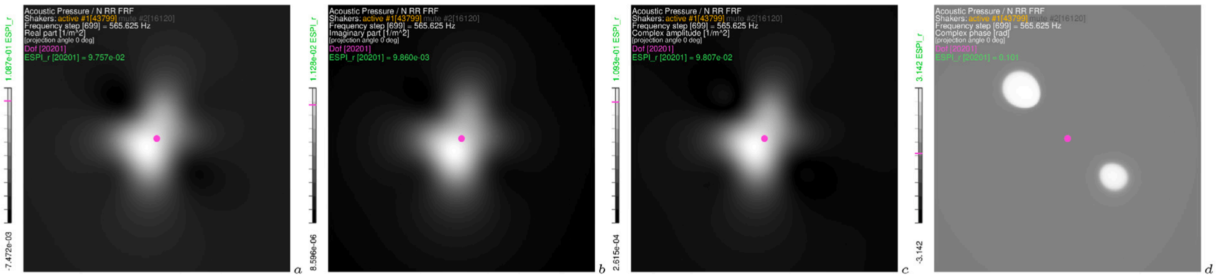

**Fig. 19.** Examples of *vibro-acoustic transfer matrix* $\boldsymbol{V}_{aS_1}(\omega)$ mesh evaluated at the specific frequency of 565.62 Hz, highlighted (magenta) acoustic dof $a = 20201$, mesh distance of 75 mm, in its parts: *real part* in $a$, *imaginary part* in $b$, *complex amplitude* in $c$ and *complex phase* in $d$.

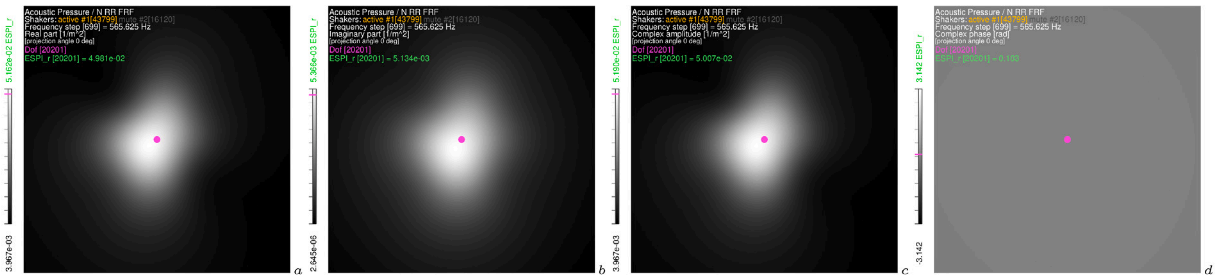

**Fig. 20.** Examples of *vibro-acoustic transfer matrix* $\boldsymbol{V}_{aS_1}(\omega)$ mesh evaluated at the specific frequency of 565.62 Hz, highlighted (magenta) acoustic dof $a = 20201$, mesh distance of 125 mm, in its parts: *real part* in $a$, *imaginary part* in $b$, *complex amplitude* in $c$ and *complex phase* in $d$.

*parts* alone of the *receptance* ODS, rather than with the *complex amplitude* and *phase* ones, where, instead, a kind of early mixing – or simplifying averaging – of the structural shape takes place. The tiles of Fig. 19 at 75 mm already show a simplified, and smoother, pattern for the *vibro-acoustic transfer matrix* $\boldsymbol{V}_{aS_1}(\omega)$. Now the *complex amplitude* in Fig. 19$c$ appears very similar to both the *real* and *imaginary parts* in Figs. 19$a,b$. Compared to Fig. 18$d$, the *complex phase* in Fig. 19$d$ flattens in the wrapping, except for two round areas, above 2 corners of the vibrating plate (which was mounted in a nearly free–free restraining condition). At the maximal distance here simulated – for the acoustic mesh – of 125 mm, the *vibro-acoustic transfer matrix* $\boldsymbol{V}_{aS_1}(\omega)$ of Fig. 20 has smoothed the main articulations of the complex pattern of the *receptance* ODS of Fig. 9. Without quantitatively precise comparative tools such as those of Modal Assurance Criterion (MAC) (Allemang, 2003), or rather of Frequency Response Assurance Criterion (FRAC) (Heylen et al., 1998; Ewins, 2000; Zanarini, 2022a), the shapes in Figs. 20$a,b,c$ now appear hardly distinguishable (except for the labels). The *complex phase* in Fig. 20$d$ is nearly flat. The same statements, about the expansion and smoothing of the *vibro-acoustic transfer matrix* pattern with the distance, continue therefore to be valid also at 565.62 Hz.

The articulation of the *receptance* pattern in Fig. 10 at 996.41 Hz is quite high, in all its $\mathbb{C}$ parts, thanks to the complex structural dynamics of the lightweight plate tested in the TEFFMA project. When fed into Eq. (15), the *receptance* pattern in Fig. 10 generates a *vibro-acoustic transfer matrix* $\boldsymbol{V}_{aS_1}(\omega)$ with clear signs of that complexity in the ODS pattern, especially at closer distances, typical of NAH (Maynard et al., 1985; Veronesi and Maynard, 1987; Williams, 1999; Mas and Sas, 2004). Therefore, prior to the expansion and smoothing of the *vibro-acoustic transfer matrix* field due to the distance in the Green functions, the tiles of Fig. 21 highlight a hyper detailed variability in the pattern, in all its parts of the data. Among them, only the *complex phase* in Fig. 21$d$ exhibits a less marked footprint of the *receptance* ODS at the centre of the acoustic mesh. Distance works in Green functions already at the intermediate distance of 75 mm of the acoustic mesh here simulated, as can be seen in Fig. 22. The active footprint on the *vibro-acoustic transfer*

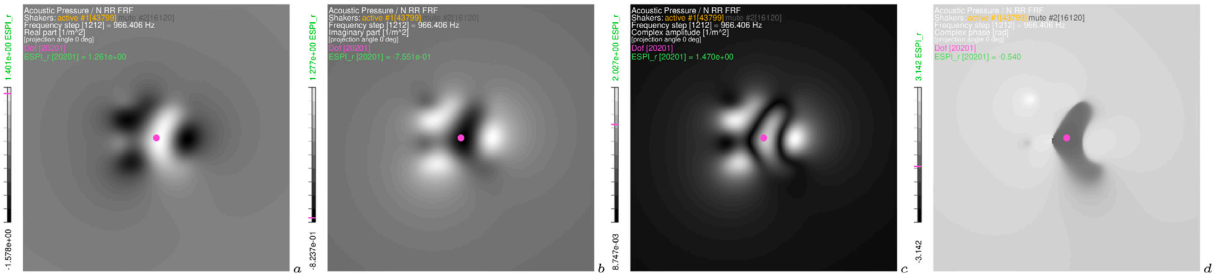

**Fig. 21.** Examples of *vibro-acoustic transfer matrix* $\boldsymbol{V}_{aS_1}(\omega)$ mesh evaluated at the specific frequency of 966.41 Hz, highlighted (magenta) acoustic dof $a = 20201$, mesh distance of 25 mm, in its parts: *real part* in $a$, *imaginary part* in $b$, *complex amplitude* in $c$ and *complex phase* in $d$.

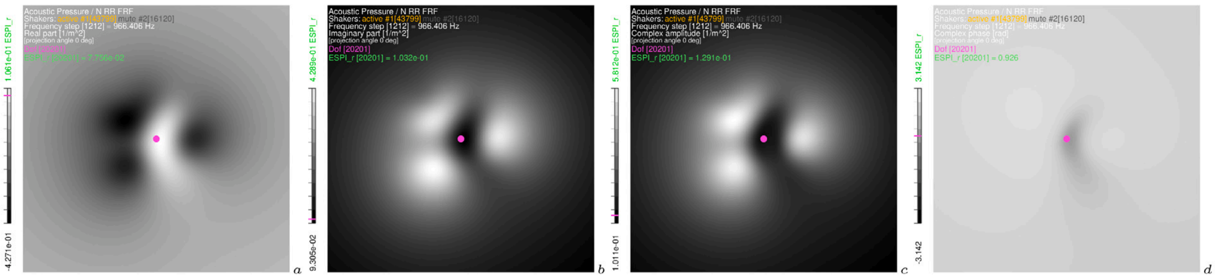

**Fig. 22.** Examples of *vibro-acoustic transfer matrix* $\boldsymbol{V}_{aS_1}(\omega)$ mesh evaluated at the specific frequency of 966.41 Hz, highlighted (magenta) acoustic dof $a = 20201$, mesh distance of 75 mm, in its parts: *real part* in $a$, *imaginary part* in $b$, *complex amplitude* in $c$ and *complex phase* in $d$.

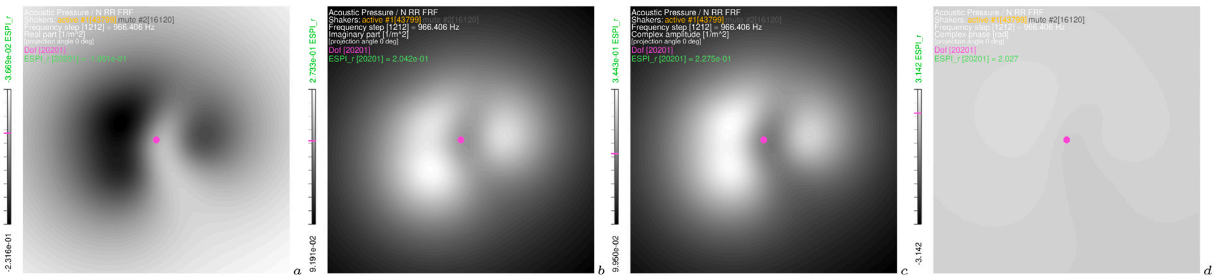

**Fig. 23.** Examples of *vibro-acoustic transfer matrix* $\boldsymbol{V}_{aS_1}(\omega)$ mesh evaluated at the specific frequency of 966.41 Hz, highlighted (magenta) acoustic dof $a = 20201$, mesh distance of 125 mm, in its parts: *real part* in $a$, *imaginary part* in $b$, *complex amplitude* in $c$ and *complex phase* in $d$.

*matrix* now covers nearly 1/2 of the mesh, showing an increased capability, of the more articulated ODS by $\omega^2$, to reach wider areas with a detailed pattern. However, by comparing the patterns in all the tiles of Fig. 22 with those in Fig. 21, it is manifest how the Green functions are strongly blending – or mixing, averaging and simplifying – the articulations of the *receptance* ODS, not only simply enlarging the patterns. But while the *real*, *imaginary parts* and *complex amplitude* of the *vibro-acoustic transfer matrix* $\boldsymbol{V}_{aS_1}(\omega)$ in Figs. 22*a*–*c* retain a distinguishable pattern, the *complex phase* in Fig. 22*d* is nearly flattened. Fig. 23 sketches the evaluation of the *vibro-acoustic transfer matrix* $\boldsymbol{V}_{aS_1}(\omega)$ at 125 mm away from the radiating surface. The footprint of the *receptance* pattern in Fig. 10 has now covered nearly the whole acoustic mesh with active contributions, but clearly the *vibro-acoustic transfer matrix* has lost that articulation in the pattern of the *receptance* source. Most of the detailed features belonging to Fig. 21, at a distance of 25 mm between structural and acoustic domains, have nearly disappeared in all the $\mathbb{C}$ data component of Fig. 23; at 125 mm, instead, with a very strong fusion of the minute details in the patterns, there is a kind of strong $\mathbb{C}$ blending operated by the Green functions at increased distance, which nearly flattens the *complex phase* in Fig. 23*d*, but also changes the patterns of the *real*, *imaginary parts* and *complex amplitude* in Figs. 23*a*–*c*.

As was already shown in Zanarini (2023b, 2024c) with SLDV- and DIC-based datasets, at closer distances the structural *receptance* ODS projects into the *vibro-acoustic transfer matrix* mesh with a much clearer reproduction of nodal lines' arrangement. Therefore, as the frequency rises, indeed more shape complexity pertains to the *receptance* maps, as can be clearly seen passing from Fig. 8 at 78.9 Hz to Fig. 9 at 565.62 Hz and to Fig. 10 at 966.41 Hz; but the resulting $\mathbb{C}$ blending in the *vibro-acoustic transfer matrix* field, taking into account all the contributions across the radiating surface, properly phased, has quite a different shape now, coming from the summation of $N_q = 49042$ contributing Green functions, in agreement with NAH (see Maynard et al. (1985), Veronesi and Maynard (1987), Williams (1999), Mas and Sas (2004)).

By means of extremely accurate[22] and *dense* ESPI-based full-field *receptances*, the evaluations of the *vibro-acoustic transfer matrix* $\boldsymbol{V}_{\boldsymbol{af}}(\omega)$ were possible and shown over the entire acoustic mesh of $N_a = 40401$ acoustic dofs with unprecedented detail from real testing. In addition to advanced vibro-acoustics, other NVH and substructuring methodologies (e.g., Heylen et al. (1998), Liu and Ewins (1999), Research network (1998), Ewins (2000), Friswell and Mottershead (1995), Haeussler et al. (2020)) may take advantage of such achievements by *dense* full-field *receptances* to improve the reliable modelling of complex structures and to enhance any benchmark for next design procedures. The experiment-based *vibro-acoustic transfer matrix* retained, therefore, the $\mathbb{C}$ relations and *phase* delays, coming from the *receptance* matrix $\boldsymbol{H}_{\boldsymbol{d}_{nqS_1}}(\omega)$ of the real testing, but blended in the summation by the Green functions. It is also manifest how the distance of the acoustic mesh plays a relevant role in blending, or fusing with fading effects, the contributions of specific areas on the vibrating plate, revealing in particular the proximity to specific nodal lines of the structural ODSs, especially at lower frequencies, therefore stressing the role of the *receptance* matrix $\boldsymbol{H}_{\boldsymbol{d}_{nqS_1}}(\omega)$, as obtained from real-life distributed damping and boundary conditions.

[22] Only ESPI was able to sense, as hinted in Zanarini (2019a), the local footprint of the impedance heads, as can be glimpsed in Figs. 9–10$a, b$ for shaker 2.

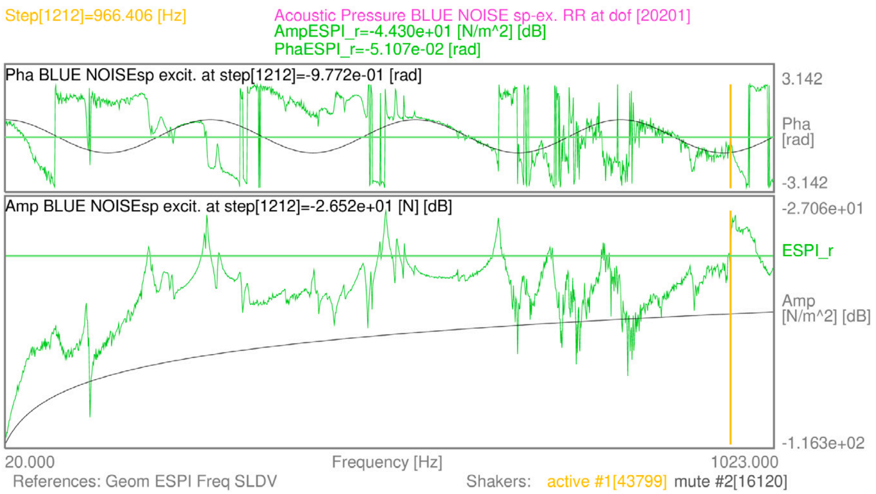


**Fig. 24.** Example of *acoustic pressure* $p(a, \omega)$ graph in the frequency domain evaluated in acoustic dof $a = 20201$, mesh distance of 75 mm, with *blue noise-sp* excitation from shaker 1.

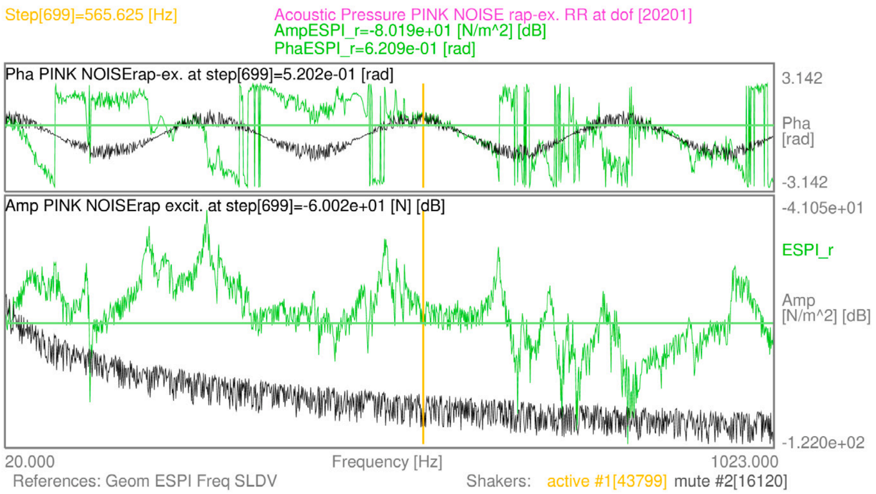


**Fig. 25.** Example of *acoustic pressure* $p(a, \omega)$ graph in the frequency domain evaluated in acoustic dof $a = 20201$, mesh distance of 75 mm, with *pink noise-rap* excitation from shaker 1.

### 5.3. Evaluation of acoustic pressure spectra from structural excitation signals

The full retention of the $\mathbb{C}$ nature of the *vibro-acoustic transfer matrix* is emphasised even more once the $\mathbb{C}$ signatures of the excitations are adopted, e.g. as modelled in Section 4, for the deployment in the whole frequency domain here analysed. For all the simulations in Sections 5.3–5.4, the distance of the acoustic mesh from the vibrating plate was fixed at 75 mm. Disregarding the *white noise* excitation – which leads only to a scaling of the data shown for the *vibro-acoustic transfer matrix* – and the $\mathbb{R}$ signatures in Eq. (17) and (19) (as already adopted and commented in Zanarini (2022c, 2023a, 2024a)), 2 signals only were meaningfully simulated here: *blue noise-sp* (in the shape of Eq. (18) with $\alpha = -1$) and *pink noise-rap* (in the shape of Eq. (20) with $\alpha = 1$), which means that both are $\mathbb{C}$ excitations, without – or with – randomness in the *complex amplitude* and *phase*. In the following 2D graphs of Figs. 24–25, the *excitation signals*, by means of black curves and text, are superimposed to the *acoustic pressure* spectra (in green). As anticipated, the black curves of the *excitation signals* are scaled in the *complex amplitude* to be restricted to 60% of the window height, while the *complex phase* maintains its values in the $[-\pi, \pi]$[rad] range. The black texts add the exact value, in its *complex valued* parts, of the *excitation signals* at the frequency of the cursor (dark yellow lines), while green texts do it for the $p(a, \omega)$. Specific labels are also added for the type of coloured noise used.

By comparing $p(a, \omega)$ in Fig. 24 to the shape of the *vibro-acoustic transfer matrix* $\boldsymbol{V}_{aS_1}(\omega)$ shown in Fig. 13, it is clear that the *blue noise-sp* excitation introduces now a combined *complex amplitude* modulation in the spectrum of the *acoustic pressure* at dof $a = 20201$, as function of the frequency dependent *amplitude*, together with the sinusoidal *phase* modification. Specifically, the *complex amplitude* of the *acoustic pressure* sees a moderate increase (in logarithmic scale) of the higher frequency components due to the *blue noise* nature (see Eq. (18) with $\alpha = -1$), while the *complex phase* of the *acoustic pressure* sees the additional contribution of the *excitation* sinusoidal *phase*, coming to a completely different spectrum. Due to its definition, the *blue noise-sp* excitation does not add any randomness in the $\mathbb{C}$ multiplication with the *vibro-acoustic transfer matrix* to obtain the *acoustic pressure* spectra.

It is again clear in Fig. 25, compared to the shape of the *vibro-acoustic transfer matrix* $\boldsymbol{V}_{aS_1}(\omega)$ shown in Fig. 13, how the *pink noise-rap* excitation introduces a *complex amplitude* scaling in the spectrum of the *acoustic pressure* $p(a, \omega)$ at dof $a = 20201$, as function of the frequency dependent *amplitude*, and specific sinusoidal *phase* modifications, leading to quite a different shape of the functions. On top of those $\mathbb{C}$ modifications, a very strong randomness is now added to both the *complex amplitude* (scattering of $\pm 50\%$) and *complex phase* (scattering of $\pm 50\%$ rad of the selected *phase* function). Additionally, the *complex amplitude* of the *acoustic pressure* sees a drop of the higher frequency components due to the *pink noise* nature (see Eq. (20) with $\alpha = 1$).

Also the evaluation of the *acoustic pressure* $p(a, \omega)$ was possible by Eq. (16), in every dof of the acoustic mesh, by means of the extremely accurate and *dense* ESPI-based full-field *receptances* $\boldsymbol{H}_{d_n}(\omega)$, of the *vibro-acoustic transfer matrix* $\boldsymbol{V}_{af}(\omega)$ and of the selected *excitation signatures*. In the whole broad frequency band here retained, this achievement was obtained with great detail, without any FEM and any approximation – nor distorting assumptions – about the behaviour of the structural domain, except for its linearity.

Furthermore, by varying the parameters in the $\mathbb{C}$ coloured noise with randomness in both the *complex amplitude* and *phase*, as that of Eq. (20), it is possible to appreciate how the whole experiment-based full-field approach is ready to be fed by real-life spectra (Bendat and Piersol, 2000), those obtainable by the estimation of actual forces on the prototypes or assembled components, without any specific approximation, but retaining the rich dynamics and *dense* details of the ESPI-based full-field *receptances* $\boldsymbol{H}_{d_n}(\omega)$.

### 5.4. Evaluation of acoustic pressure fields from structural excitation signals

The *acoustic pressure* fields $\boldsymbol{p}(\boldsymbol{a}, \omega)$ are here shown at specific frequencies in the whole acoustic mesh, or spatial domain, instead of in only the magenta dof $a = 20201$ as before, while in Section 5.3 the single-dof $p(a, \omega)$ spectra were shown in the entirely retained frequency domain of [20–1024] Hz. As in Section 5.2 for the *vibro-acoustic transfer matrix* $\boldsymbol{V}_{af}(\omega)$, the *acoustic pressure* fields $\boldsymbol{p}(\boldsymbol{a}, \omega)$ are shown in grey tones in all their components of the $\mathbb{C}$ notation: in each picture, tile $a$ contains the *real part* of the dataset, tile $b$ the *imaginary part*, tile $c$ the *complex amplitude* and tile $d$ the *complex phase*. The *excitation forces* are the same 2 signals simulated in Section 5.3: *blue noise-sp* (without any randomness, in the shape of Eq. (18) with $\alpha = -1$) and *pink noise-rap* (with strong randomness added, in the shape of Eq. (20) with $\alpha = 1$).

Starting with the *blue noise-sp* signal, Fig. 26 shows how the *vibro-acoustic transfer matrix* $\boldsymbol{V}_{\boldsymbol{a}S_1}(\omega)$ of Fig. 16 is influenced by the $\mathbb{C}$ excitation, without any randomness, at 78.9 Hz. The nature of the excitation interacts with the multiplication of the *vibro-acoustic transfer matrix* $\boldsymbol{V}_{\boldsymbol{a}S_1}(\omega)$ data parts. It is manifest how, in particular, a change in the mapping of $\boldsymbol{p}(\boldsymbol{a}, \omega)$ happens in the *complex phase*: the latter rises – the whole map is uniformly shifted up in the range – by 0.194 rad between the *complex phase* in Fig. 16*d* and that in Fig. 26*d*, evaluated by the *phase* differences in the magenta dof $a = 20201$, respectively equal to −2.881 rad and −2.687 rad. But being the *complex phase* wrapped in the range $[-\pi, \pi]$ rad (what is raised beyond $\pi$ rad gets a $-2\pi$ rad addition, and vice-versa), it is represented in deepest tones of grey instead of bright tones of grey, as it appears lifted in Fig. 26*d*, restarting at the bottom of the wrapped range, or reducing the brighter areas. Furthermore, the relative mapping of the *complex phase* in the mesh is not touched by this uniform shift, as expected since the excitation is from a single shaker. The scaling by the *blue noise-sp* excitation does not touch – at least apparently, in a clear manner due to the limited, but uniform, *phase* shift – either the relative mapping of the *real part*, of the *imaginary part* or of the *complex amplitude* of $\boldsymbol{p}(\boldsymbol{a}, \omega)$, therefore the couples of Figs. 16*a*–26*a*, of Figs. 16*b*–26*b* and of Figs. 16*c*–26*c* appear with the same relative mapping in the mesh, albeit from different physical quantities and absolute values.

Other comparisons with *blue noise-sp* excitation are taken at 565.62 Hz between the *pressure* fields $\boldsymbol{p}(\boldsymbol{a}, \omega)$ in Fig. 27 and the *vibro-acoustic transfer matrix* $\boldsymbol{V}_{\boldsymbol{a}S_1}(\omega)$ in Fig. 19, reminding the reader that in the latter there was already quite a similarity among the tiles $a$–$c$, induced by the flatness of the *complex phase* in tile $d$. With attention again to the *complex phase*, a shift of 0.973 rad can be appreciated between Fig. 27$d$ and Fig. 19$d$: with the wrapping in the range $[-\pi, \pi]$ rad – what is raised above $\pi$ rad gets a $2\pi$ rad subtraction – the top of the bright areas in Fig. 19$d$ are now darkened at the bottom of the range, with an annular bright area of the locations raised just at the top of the range.

The last comparisons with *blue noise-sp* excitation are taken at 996.41 Hz between the *pressure* fields $\boldsymbol{p}(\boldsymbol{a}, \omega)$ in Fig. 28 and the *vibro-acoustic transfer matrix* $\boldsymbol{V}_{\boldsymbol{a}S_1}(\omega)$ in Fig. 22. There is not a manifest relative change in the shape of the *complex phase* between Figs. 22$d$, 28$d$, as well as in the relative shape of the *complex amplitude* between Figs. 22$c$, 28$c$. Although now the *complex phase* – down-shifted by 0.977 rad – is not affected by the wrapping in the range $[-\pi, \pi]$ rad, the newly induced *phase*, due to its more pronounced relative articulation, does change the projection of the *real* and *imaginary parts*, now with a grey tone shift of the *real part* between Figs. 22$a$, 28$a$, paired with a sign change in the *imaginary part* between Figs. 22$b$, 28$b$.

Instead, in Fig. 29 at 78.9 Hz, the randomness in the *complex amplitude* and *phase* of the *pink noise-rap* excitation signal brings a new $\mathbb{C}$ scaling of the *vibro-acoustic transfer matrix* $\boldsymbol{V}_{\boldsymbol{a}S_1}(\omega)$ of Fig. 16. While the same approach followed in the discussion about Fig. 26 can be recalled, here in Fig. 29 the randomness adds a different $\mathbb{C}$ scaling factor, therefore the $a, b$ maps (*real* & *imaginary parts*) have slight changes, as can be appreciated also by the magenta bar in the ranges, with shifts that are different (albeit limited, with no changes in the *complex amplitude* in tile $c$, as expected), but particularly manifest among only the relative mapping of the *complex phases* of Fig. 29$d$ against Fig. 16$d$ with a slightly greater *phase* shift of 0.245 rad. The latter reduces the bright areas in the pattern further, due to the wrapping of the *phase*, but does not change the relative shape.

The *phase* shift of 0.52 rad by the *pink noise-rap* excitation signal at 565.62 Hz is now less than before with the other *blue noise-sp* forcing signal. The change in the wrapping between $\boldsymbol{V}_{\boldsymbol{a}S_1}(\omega)$ in Fig. 19$d$ and $\boldsymbol{p}(\boldsymbol{a}, \omega)$ in Fig. 30$d$ now involves a slightly reduced

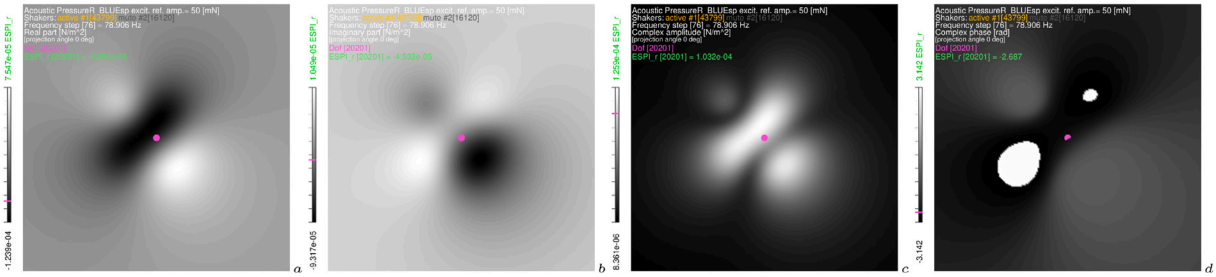

**Fig. 26.** Examples of *acoustic pressure* mesh evaluated at the specific frequency of 78.9 Hz, highlighted (magenta) acoustic dof 20201, *blue noise-sp* excitation from shaker 1, mesh distance of 75 mm, in its parts: *real part* in $a$, *imaginary part* in $b$, *complex amplitude* in $c$ and *complex phase* in $d$.

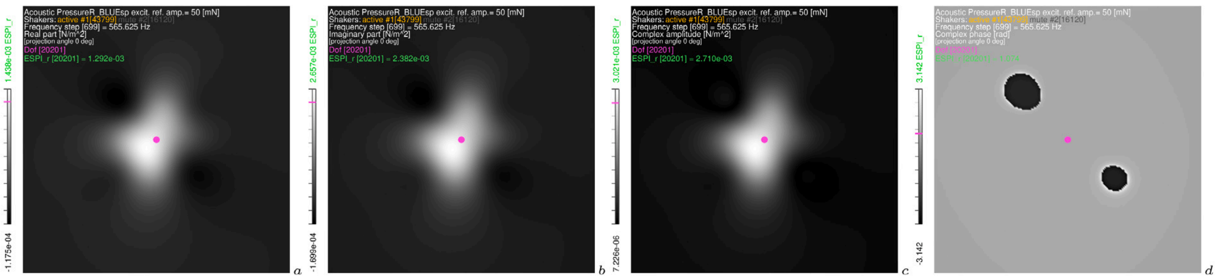

**Fig. 27.** Examples of *acoustic pressure* mesh evaluated at the specific frequency of 565.62 Hz, highlighted (magenta) acoustic dof 20201, *blue noise-sp* excitation from shaker 1, mesh distance of 75 mm, in its parts: *real part* in $a$, *imaginary part* in $b$, *complex amplitude* in $c$ and *complex phase* in $d$.

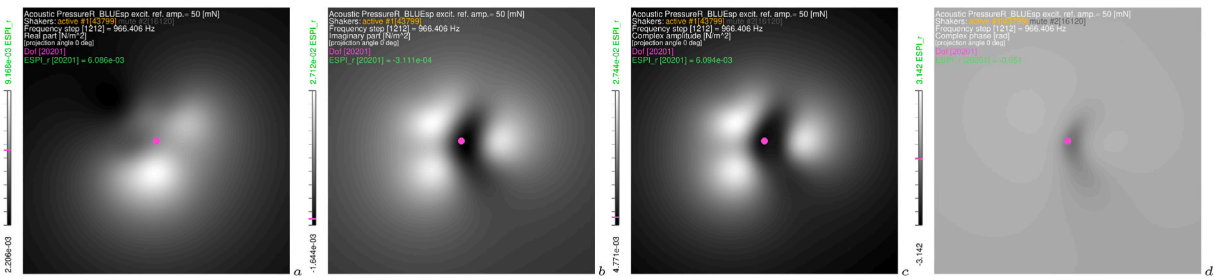

**Fig. 28.** Examples of *acoustic pressure* mesh evaluated at the specific frequency of 996.41 Hz, highlighted (magenta) acoustic dof 20201, *blue noise-sp* excitation from shaker 1, mesh distance of 75 mm, in its parts: *real part* in $a$, *imaginary part* in $b$, *complex amplitude* in $c$ and *complex phase* in $d$.

portion of the bright areas. No other manifest change can be reported in the relative mapping of the *real*, *imaginary* and *complex amplitude* parts of $\boldsymbol{p}(\boldsymbol{a},\omega)$ in Figs. 30*a*, *b*, *c*, respectively.

At 996.41 Hz, the newly shaped $\mathbb{C}$ scaling, given by the *pink noise-rap* excitation, affects markedly the projection of the *real* and *imaginary parts* of $\boldsymbol{p}(\boldsymbol{a},\omega)$, but without manifest changes in the relative mapping of the *complex amplitude* and *phase*, apart from uniform scaling and shifting (inside the *phase* wrapping, with uniform darkening), respectively, from $\boldsymbol{V}_{\boldsymbol{a}S_1}(\omega)$. Therefore the couples of Figs. 31*a*, 22*a* and of Figs. 31*b*, 22*b* are clearly different in the patterns and toning. Instead, in the couple of Figs. 31*c*, 22*c* no change is manifest, as expected, the $\mathbb{C}$ scaling being just a single rotation in the *complex plane* of the cloud of dofs' values, as hinted in Section 2.1.1. In the couple of Figs. 31*d*, 22*d*, not affected by any wrapping issue, there is surely a general darkening of the tones, but any relative change is hardly noticeable, or not easily detectable without proper numerical tools – such as MAC and FRAC maps extended to $\mathbb{C}$ datasets, as widely used instead in Zanarini (2022a, 2023b) – to compare the quite different results in the same spatial field.

### 5.5. General discussions and suggestions

Here is proposed a more general point of view about the achievements shown by the minute details in Sections 5.1–5.4, thanks to the simulations there analysed and to what advanced in all the other Sections.

By means of a rigorous $\mathbb{C}$ formulation of all the steps involved in both spatial and frequency fully populated domains, as underlined in many parts of this paper, it was possible in Sections 5.2–5.4 to obtain accurate and *dense* vibro-acoustic hybrid

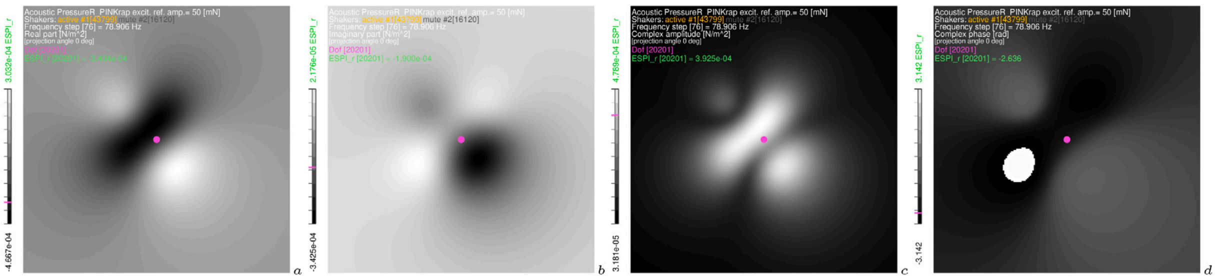

**Fig. 29.** Examples of *acoustic pressure* mesh evaluated at the specific frequency of 78.9 Hz, highlighted (magenta) acoustic dof 20201, *pink noise-rap* excitation from shaker 1, mesh distance of 75 mm, in its parts: *real part* in *a*, *imaginary part* in *b*, *complex amplitude* in *c* and *complex phase* in *d*.

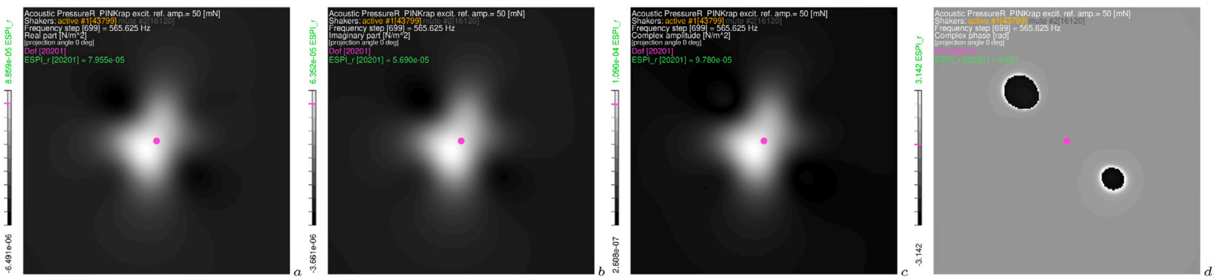

**Fig. 30.** Examples of *acoustic pressure* mesh evaluated at the specific frequency of 565.62 Hz, highlighted (magenta) acoustic dof 20201, *pink noise-rap* excitation from shaker 1, mesh distance of 75 mm, in its parts: *real part* in *a*, *imaginary part* in *b*, *complex amplitude* in *c* and *complex phase* in *d*.

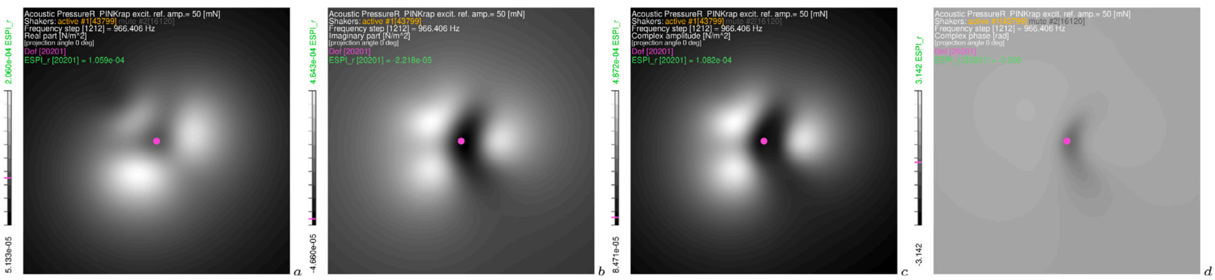

**Fig. 31.** Examples of *acoustic pressure* mesh evaluated at the specific frequency of 996.41 Hz, highlighted (magenta) acoustic dof 20201, *pink noise-rap* excitation from shaker 1, mesh distance of 75 mm, in its parts: *real part* in *a*, *imaginary part* in *b*, *complex amplitude* in *c* and *complex phase* in *d*.

simulations, with no use of pure numerical models like FEMs, but, instead, of advanced ESPI-based *receptance* datasets[23] from the real testing, with all its conditions, which might be hardly replicable by other synthetic approaches. The latter follow, most of the times, a $\mathbb{R}$ numerical processing, therefore they are not able to precisely handle the real-life structural dynamics, but just a simplifying projection of it, loosing the phase relationships stored in the $\mathbb{C}$ formulation of the broad frequency band quantities, as was also underlined in Section 2, with added specific details in Section 2.1.1. Also, the evaluation of synthetic *receptances* in a broad frequency band is generally more demanding with the complete structural (mass, damping, stiffness) matrices of a FEM, instead of using a truncated modal base, even if not fully tuned. On the contrary, note that no residual errors are here kept from interpolations nor EFFMA identifications (e.g. as in Zanarini (2019b)), remarking how the ESPI-based *receptances* are a very sensitive – with extremely low noise in the data field – technique for dynamic testing of hardly modellable ODSs' patterns. Stroboscopic $\mathbb{C}$ ESPI, however, has the marked drawback of time-consuming acquisitions, therefore better suited for mission-critical parts, whose modelling cannot be fully refined with other cheaper approaches.

The $\mathbb{C}$ reformulation of the Rayleigh integral approximation in Section 3 worked flawlessly and independently of the detail simulated in the acoustic mesh and frequency domain, the only restraint[24] being the computing facility, but with relatively limited time-consuming simulations in comparison to the testing campaign. Note that everything was achieved without further assumptions, but with high detail, in the spatial and frequency domains, thanks to the quality of the raw *dense* $\mathbb{C}$ ESPI-based optical full-field *receptances* and to the introduced (in Section 4) $\mathbb{C}$ representation of the excitation signature, able to address any real-life forcing spectrum. *Dense* stroboscopic $\mathbb{C}$ ESPI-based optical full-field *receptances* have proved to give a reliable source for the most demanding structural dynamics of a vibrating surface in vibro-acoustic diffusion approximation. The quality of the achievements was supported by the proper $\mathbb{C}$ numerical handling of all the quantities, in the processing and representation, by means of the custom C-language coding, using `double float` numbers, OpenMP (parallelisation) and OpenGL (graphics) libraries. Under the specific testing conditions of this work, this approach pushes the boundaries of the conclusion "*[..] the more complex the source is, the more accurate results can be obtained*", made 40 years ago by Augusztinovicz et al. (1995). Furthermore, new hybrid 3D ESPI-based vibro-acoustic approaches can be designed in the future, starting from the proved achievements, for even more articulated scenarios of manifold surfaces in radiating structures and boundary conditions.

Suggestions about the correct climate conditions were already made in Section 5.1, but should here be recalled with an extension in mind: that of the coupling with other fluids, either gases or liquids, generally having their specific relation with the climate conditions, like temperature, humidity, viscosity, concentrations, etc., as also hinted in Section 3.1, but respecting the conditions of Eq. (11). Therefore, with the due attentions to the reproducibility – e.g. in anechoic climatic chambers/basins and/or specifically under control ones – of conditions in the testing, the proposed approach might evaluate the vibro-acoustics also in the broad cases of general fluid–structure interactions. This because a new fluid certainly affects the sound pressure waves diffusion in the medium, but might change particularly the generalised damping on the surface and of the components, thus specific testing – e.g. for submerged structures in water – is required with all the controlled parameters, stroboscopic $\mathbb{C}$ ESPI-based measurements remaining at the core of this approach.

Starting from Section 2, and later from Section 3, it is well underlined (as in Zanarini (2019a)) that the proposed vibro-acoustic approach is based on the linearity assumption, about the relation between the excitation on the structure and the related responses. Also potential non-linear structural behaviours are linearised around the specific conditions of the testing, which needs to be made accordingly to the vibro-acoustic scenario that is later targeted by the simulations of $\boldsymbol{V}_{af}(\omega)$ and of $p(\boldsymbol{a}_a, \omega)$. Furthermore, it is of uttermost relevance to underline that if the excitation level from Section 4 changes upto breaking the linearity assumption, new structural testing must be made, in order to have the structural dynamics newly linearised around the new conditions. But, due to the long lasting accurate stroboscopic $\mathbb{C}$ ESPI-based measurements, the suggestion, left for future researches, can be to reproduce properly – thus with previous precise estimation[25] in the desired broad frequency band – the wanted excitation level in the stepped-sine laboratory testing.

Despite the achievements here underlined, however, extended checks and proofs of the experiment-based vibro-acoustic procedure are suggested in the future, as it was not possible during the TEFFMA project, which remained limited to the comparison of the different techniques for full-field non-contacting vibration testing, as summarised in Section 2. Therefore, the acoustic side of the testing deserves more attention in future researches, to obtain the acoustic measurements in a set-up resembling the mesh of $p(\boldsymbol{a}_a, \omega)$, radiated by the vibrating surface, as was made in Maynard et al. (1985), Veronesi and Maynard (1987), Coster et al. (2010),

[23] Already in Section 1 was recalled that ESPI can successfully sense very articulated vibration patterns up to several kHz.

[24] Indeed, it must be recalled that the same ESPI-based datasets here used might bring to much denser grids of structural dofs, because, in the phase map unwrapping process of the stroboscopic $\mathbb{C}$ ESPI-based virtual field as in Section 2.1.1 the interpolation was limited to only 250 × 250 dofs, later limited to the internal 226 × 217 *receptance* map dofs. The acoustic mesh of Section 5.1 could have been even more detailed than 201 × 201 dofs, but with limited aid to explain the approach further. The *vibro-acoustic transfer matrix* $\boldsymbol{V}_{af}(\omega)$, as well as the *pressure* fields $p(\boldsymbol{a}_a, \omega)$ by proper $\mathbb{C}$ excitation spectra, could be shown in even denser spatial domain simulations. This trade-off was made to handle the datasets with relatively low memory allocations (below the max of 192 GB of RAM at disposal for this research) and be able to compute the vibro-acoustic simulation in a few tens of minutes. The approach is only limited by the computing facility, rather than by the testing conditions, but it can already get the advancement of the very accurate structural ODSs' description from ESPI with its *dense* $\mathbb{C}$ sensing, which might be hardly matched by other measurement techniques.

[25] E.g. by means of the TPA in Van der Auweraer et al. (2008), Gajdatsy et al. (2010), de Klerk and Rixen (2010), van der Seijs et al. (2016), Cumbo et al. (2019), Ortega Almirón et al. (2022), or by the approaches coming from Frequency Based Substructuring (FBS) as in Voormeeren et al. (2010), Wagner et al. (2020), Haeussler et al. (2020), Pogacar et al. (2022), or from Multi Input Multi Output (MIMO) vibration testing in Vaes et al. (2005), Musella et al. (2017), Schumann et al. (2022).

Squicciarini et al. (2015), Wagner et al. (2020), Ortega Almirón et al. (2022). More attention is deserved also by the close surfaces, to reduce even further the potential sound waves' reflections in the frequency range of interest, as underlined in Sections 2.1 and 3. If possible, the test rig – used by the ESPI-based optical techniques – should be positioned in a (semi-)anechoic chamber, with a preferred floating floor to assure the ground vibrations' insulation. A practical suggestion for the *acoustic pressure* field mapping is to adopt a microphone array, with a relatively coarse grid to prevent relevant distortions on the acoustic signal by the dimension of each microphone and fixture, and to move the array – parallel to the surface – by fractions of its grid spacing, in the same way as it was arranged in acoustic beamforming campaigns (e.g. in Castellini and Martarelli (2008), Du and Morris (2015), Leclère et al. (2017), Chiariotti et al. (2019)), to obtain a spatially oversampled description of both $p(\boldsymbol{a_a}, \omega)$ and $\boldsymbol{V_{af}}(\omega)$, up to the desired spatial detail, as comparable to the meshing of Section 5.1, later used for all the simulations in Sections 5.2–5.4. For an even stronger validation of the $\boldsymbol{V_{af}}(\omega)$ in Eq. (16), volume velocity sources, as in Augusztinovicz et al. (1995) or as in the author's experiences[26], might be of aid, under the reciprocity principle, to confirm the inverse relation.

But all the suggested future researches, made in controlled environments for all the parameters involved in vibro-acoustics, can be the first step to foster a broader applicability of the techniques to more complex mission-critical parts and advanced hybrid simulation methodologies, especially when traditional simulation tools (e.g. FEM) have tuning issues or when enhanced and spatially detailed experiment-based benchmarks are needed to advance the reality's comprehension.

## 6. Conclusions

This work underlined the benefits coming from spatially *dense* stroboscopic *complex-valued* ESPI-based optical full-field *receptances* in frequency domain vibro-acoustics, bringing hyper-detailed real-life experiment-based structural dynamics. Specifically, by means of the well-known Rayleigh integral approximation of sound propagation due to a vibrating surface once excited by broad frequency band forces, a high-quality experiment-based mapping ability was achieved in simulating *vibro-acoustic transfer matrices* and *acoustic pressure* fields. The possibilities in vibro-acoustics coming from experiment-based optical full-field tools, by the case of the *dense* and precise ESPI measurements, were underlined at their maximal spatial detail and accuracy obtainable nowadays, but methodologically open to future extensions.

That enhanced mapping ability – in both spatial and frequency domains – targets novel hybrid vibro-acoustic prediction paradigms without the need of FEM, the complete *complex-valued* real-life structural dynamics of the radiating surface being entirely retained in the vibro-acoustic simulation with great accuracy and details, but without assumptions in the damping, nor errors in unneeded identifications nor model updating, nor inertia distortions in the measurements of lightweight structures, nor smoothing of the data. Furthermore, these experiment-based full-field techniques can provide new benchmarks for improving the simulations from any synthetic model, for a clear advancement of design procedures and of virtual prototyping of complex structures and mission-critical components, hardly manageable by other techniques.

New experiments are needed to verify these hybrid sound radiation predictions, and to give further assurance of the achieved results in the future, for an increased awareness of full-field measurements' capabilities for the most demanding vibro-acoustic radiation predictions. Experiment-based optical full-field NVH, nonetheless, is on an encouraging path, paved with promising advancements coming from growing image-based approaches.

## Declaration of competing interest

The authors declare that they have no known competing financial interests or personal relationships that could have appeared to influence the work reported in this paper.

## Acknowledgements

This activity is a spin-off of the TEFFMA (Towards Experimental Full Field Modal Analysis) project, funded by the European Commission at the Technische Universitaet Wien, through the Marie Curie FP7-PEOPLE-IEF-2011 PIEF-GA-2011-298543 grant, for which the Research Executive Agency is greatly acknowledged. TU-Wien, in the person of Professor Wassermann and his staff, are kindly acknowledged for having hosted the TEFFMA project of the author at the *Schwingungs- und Strukturanalyse / Optical Vibration Measurement Laboratory*. The Linux-based workstation, used to extensively process the datasets and code in C-language/OpenMP/OpenGL the whole outputs, was provided by the author out of his own savings. Professor Roberta Mullini is wholeheartedly acknowledged for her care in the proofreading of the English text.

## Data availability

The data that has been used is confidential.

[26] The author gained experience in vibro-acoustics since the European Commission HPMT-CT-2000-00034 Marie Curie Host Fellowship project *Hybrid modelling for road noise predictions*, at KU Leuven in 2002, which brought to the paper Direct and indirect vibro-acoustic measurements for road noise NVH predictions.

## References


Abdelkefi, A., 2016. Aeroelastic energy harvesting: A review. Internat. J. Engrg. Sci. 100, 112–135. http://dx.doi.org/10.1016/j.ijengsci.2015.10.006.

Afonso, F., Vale, J., Oliveira, É., Lau, F., Suleman, A., 2017. A review on non-linear aeroelasticity of high aspect-ratio wings. Prog. Aerosp. Sci. 89, 40–57. http://dx.doi.org/10.1016/j.paerosci.2016.12.004.

Allemang, R.J., 2003. The modal assurance criterion – twenty years of use and abuse. Sound Vib. 37 (8), 14–23, URL: http://www.sandv.com/downloads/0308alle.pdf.

Allen, M.S., Sracic, M.W., 2010. A new method for processing impact excited continuous-scan laser Doppler vibrometer measurements. Mech. Syst. Signal Process. 24 (3), 721–735. http://dx.doi.org/10.1016/j.ymssp.2009.11.004.

Arenas, J.P., 2008. Numerical computation of the sound radiation from a planar baffled vibrating surface. J. Comput. Acoust. 16 (03), 321–341. http://dx.doi.org/10.1142/S0218396X08003671.

Augusztinovicz, F., Penne, F., Sas, P., 1995. Calculation of sound radiation from sources, characterized by the equivalent power volume velocity method. In: Proceedings of the 2nd Worldwide SYSNOISE Users Meeting. pp. 1–9, URL: https://last.hit.bme.hu/download/fulop/Publikaciok/2ndSYSUsrMtg-EPVV.pdf.

Baqersad, J., Poozesh, P., Niezrecki, C., Avitabile, P., 2017. Photogrammetry and optical methods in structural dynamics – A review. Mech. Syst. Signal Process. 86, 17–34. http://dx.doi.org/10.1016/j.ymssp.2016.02.011, Full-field, non-contact vibration measurement methods: comparisons and applications.

Bendat, J.S., Piersol, A.G., 2000. Random Data: Analysis and Measurement Procedures, third ed. John Wiley & Sons Inc, ISBN 9780471317333.

Bornert, M., Brémand, F., Doumalin, P., Dupré, J.-C., Fazzini, M., Grédiac, M., Hild, F., Mistou, S., Molimard, J., Orteu, J.-J., Robert, L., Surrel, Y., Vacher, P., Wattrisse, B., 2009. Assessment of digital image correlation measurement errors: Methodology and results. Exp. Mech. 49 (3), 353–370. http://dx.doi.org/10.1007/s11340-008-9204-7.

Bueno, D.D., Góes, L.C.S., Gonçalves, P.J.P., 2015. Flutter analysis including structural uncertainties. Meccanica 50, 2093–2101. http://dx.doi.org/10.1007/s11012-015-0138-8.

Calvi, A., 2005. Uncertainty-based loads analysis for spacecraft: Finite element model validation and dynamic responses. Comput. Struct. 83 (14), 1103–1112. http://dx.doi.org/10.1016/j.compstruc.2004.11.019, Uncertainties in Structural Mechanics and Analysis–Computational Methods.

Castellini, P., Martarelli, M., 2008. Acoustic beamforming: Analysis of uncertainty and metrological performances. Mech. Syst. Signal Process. 22 (3), 672–692. http://dx.doi.org/10.1016/j.ymssp.2007.09.017.

Chen, X., Qiu, Z., Wang, X., Li, Y., Wang, R., 2017. Uncertain reduced-order modeling for unsteady aerodynamics with interval parameters and its application on robust flutter boundary prediction. Aerosp. Sci. Technol. 71, 214–230. http://dx.doi.org/10.1016/j.ast.2017.09.018.

Chen, Z., Zhao, Y., Huang, R., 2019. Parametric reduced-order modeling of unsteady aerodynamics for hypersonic vehicles. Aerosp. Sci. Technol. 87, 1–14. http://dx.doi.org/10.1016/j.ast.2019.01.035.

Chiariotti, P., Martarelli, M., Castellini, P., 2019. Acoustic beamforming for noise source localization - Reviews, methodology and applications. Mech. Syst. Signal Process. 120, 422–448. http://dx.doi.org/10.1016/j.ymssp.2018.09.019.

Citarella, R., Federico, L., Cicatiello, A., 2007. Modal acoustic transfer vector approach in a FEM-BEM vibro-acoustic analysis. Eng. Anal. Bound. Elem. 31 (3), 248–258. http://dx.doi.org/10.1016/j.enganabound.2006.09.004.

Conta, S., Santoni, A., Homb, A., 2020. Benchmarking the vibration velocity-based measurement methods to determine the radiated sound power from floor elements under impact excitation. Appl. Acoust. 169, 107457. http://dx.doi.org/10.1016/j.apacoust.2020.107457.

Coster, C., Nagahata, D., van der Linden, P.J.G., 2010. On the accuracy reciprocal and direct vibro-acoustic transfer-function measurements on vehicles for lower and medium frequencies. In: Proceedings of the 24th International Conference on Noise and Vibration Engineering (ISMA2010) Conference. pp. 3873–3886, URL: https://past.isma-isaac.be/downloads/isma2010/papers/isma2010_0243.pdf.

Cumbo, R., Tamarozzi, T., Janssens, K., Desmet, W., 2019. Kalman-based load identification and full-field estimation analysis on industrial test case. Mech. Syst. Signal Process. 117, 771–785. http://dx.doi.org/10.1016/j.ymssp.2018.08.045.

de Groot, P.J., 1995. Vibration in phase-shifting interferometry. J. Opt. Soc. Amer. A 12 (2), 354–365. http://dx.doi.org/10.1364/JOSAA.12.000354.

de Klerk, D., Rixen, D., 2010. Component transfer path analysis method with compensation for test bench dynamics. Mech. Syst. Signal Process. 24 (6), 1693–1710. http://dx.doi.org/10.1016/j.ymssp.2010.01.006.

Deckers, E., Atak, O., Coox, L., D'Amico, R., Devriendt, H., Jonckheere, S., Koo, K., Pluymers, B., Vandepitte, D., Desmet, W., 2014. The wave based method: An overview of 15 years of research. Wave Motion 51 (4), 550–565. http://dx.doi.org/10.1016/j.wavemoti.2013.12.003, Innovations in Wave Modelling.

Desmet, W., 1998. A Wave-Based Prediction Technique for Coupled Vibro- Acoustic Analysis (Ph.D. thesis). Katholieke University of Leuven, Belgium, URL: https://www.mech.kuleuven.be/en/doctorates/desmet.pdf.

Desmet, W., 2004. Boundary Element Method in Acoustics. Tech. rep., Katholieke Universiteit Leuven, Belgium, Mechanical Engineering Department, Noise & Vibration Research Group, URL: https://www.mech.kuleuven.be/en/research/. In ISAAC 15 - Course on numerical and applied acoustics, Katholieke Universiteit Leuven, Belgium, Mechanical Engineering Department, Noise & Vibration research group, URL: https://www.isma-isaac.be.

Di Maio, D., Castellini, P., Martarelli, M., Rothberg, S., Allen, M.S., Zhu, W.D., Ewins, D.J., 2021. Continuous Scanning Laser Vibrometry: A raison d'être and applications to vibration measurements. Mech. Syst. Signal Process. 156, 107573. http://dx.doi.org/10.1016/j.ymssp.2020.107573.

Di Maio, D., Ewins, D.J., 2011. Continuous scan, a method for performing modal testing using meaningful measurement parameters; Part I. Mech. Syst. Signal Process. 25 (8), 3027–3042. http://dx.doi.org/10.1016/j.ymssp.2011.05.018.

Doval, Á.F., 2000. A systematic approach to TV holography. Meas. Sci. Technol. 11 (1), R1–R36, IOP Pub Ltd.

Dowell, E.H., Hall, K.C., 2001. Modeling of fluid-structure interaction. Annu. Rev. Fluid Mech. 33 (Volume 33, 2001), 445–490. http://dx.doi.org/10.1146/annurev.fluid.33.1.445.

Du, Y., Morris, P.J., 2015. The separation of radiating and non-radiating near-field pressure fluctuations in supersonic jets. J. Sound Vib. 355, 172–187. http://dx.doi.org/10.1016/j.jsv.2015.06.020.

Ehrhardt, D.A., Allen, M.S., Yang, S., Beberniss, T.J., 2017. Full-field linear and nonlinear measurements using continuous-scan laser Doppler vibrometry and high speed three-dimensional digital image correlation. Mech. Syst. Signal Process. 86 (Part B), 82–97. http://dx.doi.org/10.1016/j.ymssp.2015.12.003.

Ewins, D.J., 2000. Modal Testing - Theory, Practice and Application, second ed. Research Studies Press Ltd, Baldock, Hertfordshire, England, p. 400, ISBN 978-0-86380-218-8. URL: https://www.wiley.com/en-it/Modal+Testing%3A+Theory%2C+Practice+and+Application%2C+2nd+Edition-p-9780863802188.

Fahy, F., 2003. Foundations of Engineering Acoustics. Academic Press, London, p. 443. http://dx.doi.org/10.1016/B978-0-12-247665-5.X5000-0.

Friswell, M., Mottershead, J.E., 1995. Finite element model updating in structural dynamics. In: Solid Mechanics and Its Applications, Kuwler Academic Publishers, Springer Netherlands, p. 292, ISBN 978-0-7923-3431-6.

Gajdatsy, P., Janssens, K., Desmet, W., Van der Auweraer, H., 2010. Application of the transmissibility concept in transfer path analysis. Mech. Syst. Signal Process. 24 (7), 1963–1976. http://dx.doi.org/10.1016/j.ymssp.2010.05.008, Special Issue: ISMA 2010.

Georgas, P.J., Schajer, G.S., 2012. Modulo-2pi phase determination from individual ESPI images. Opt. Lasers Eng. 50 (8), 1030–1035. http://dx.doi.org/10.1016/j.optlaseng.2012.03.005, Fringe Analysis Methods & Applications.

Gérard, F., Tournour, M., Masri, N., Cremers, L., Felice, M., Selmane, A., 2002. Acoustic transfer vectors for numerical modeling of engine noise. Sound Vib. 36, 20–25, URL: http://www.sandv.com/downloads/0207gera.pdf.

Giuliani, P., Di Maio, D., Schwingshackl, C.W., Martarelli, M., Ewins, D.J., 2013. Six degrees of freedom measurement with continuous scanning laser doppler vibrometer. Mech. Syst. Signal Process. 38 (2), 367–383. http://dx.doi.org/10.1016/j.ymssp.2013.01.004.

Graham, G., Petzing, J., Lucas, M., 1999. Extracting modal parameters of ultrasonic bar horns from ESPI FRF data. Ultrasonics 37 (3), 231–238. http://dx.doi.org/10.1016/S0041-624X(98)00051-1.

Haeussler, M., Klaassen, S., Rixen, D., 2020. Experimental twelve degree of freedom rubber isolator models for use in substructuring assemblies. J. Sound Vib. 474, 115253. http://dx.doi.org/10.1016/j.jsv.2020.115253.

Helfrick, M.N., Niezrecki, C., Avitabile, P., Schmidt, T., 2011. 3D digital image correlation methods for full-field vibration measurement. Mech. Syst. Signal Process. 25 (3), 917–927. http://dx.doi.org/10.1016/j.ymssp.2010.08.013.

Heylen, W., Lammens, S., Sas, P., 1998. Modal Analysis Theory and Testing, second ed. Katholieke Universiteit Leuven, Leuven (Belgium), ISBN 90-73802-61-X.

Huntley, J.M., 1998. Suppression of phase errors from vibration in phase-shifting interferometry. J. Opt. Soc. Amer. A 15 (8), 2233–2241. http://dx.doi.org/10.1364/JOSAA.15.002233.

Jones, E.M.C., Iadicola, M.A. (Eds.), 2018. A Good Practices Guide for Digital Image Correlation. International Digital Image Correlation Society, http://dx.doi.org/10.32720/idics/gpg.ed1.

Kamakoti, R., Shyy, W., 2004. Fluid–structure interaction for aeroelastic applications. Prog. Aerosp. Sci. 40 (8), 535–558. http://dx.doi.org/10.1016/j.paerosci.2005.01.001.

Kirkup, S., 1994. Computational solution of the acoustic field surrounding a baffled panel by the Rayleigh integral method. Appl. Math. Model. 18 (7), 403–407. http://dx.doi.org/10.1016/0307-904X(94)90227-5.

Kirkup, S., 2019. The boundary element method in acoustics: A survey. Appl. Sci. 9 (8), http://dx.doi.org/10.3390/app9081642.

Kirkup, S., Thompson, A., 2007. Computing the acoustic field of a radiating cavity by the boundary element - Rayleigh integral method (BERIM). In: Ao, S.I., Gelman, L., Hukins, D.W.L., Hunter, A., Korsunsky, A.M. (Eds.), World Congress on Engineering, WCE 2007, London, UK, July 2-4 , 2007. In: Lecture Notes in Engineering and Computer Science, Newswood Limited, pp. 1401–1406, URL: http://www.kirkup.info/publications/SKAT07.pdf.

Kreis, T., 2004. Handbook of Holographic Interferometry: Optical and Digital Methods. Wiley-VCH, Berlin, Germany, http://dx.doi.org/10.1002/3527604154.

LeBlanc, B., Niezrecki, C., Avitabile, P., Sherwood, J., Chen, J., 2012. Surface stitching of a wind turbine blade using digital image correlation. In: Allemang, R., De Clerck, J., Niezrecki, C., Blough, J. (Eds.), Topics in Modal Analysis II, Volume 6. Springer New York, New York, NY, pp. 277–284. http://dx.doi.org/10.1007/978-1-4614-2419-2_27.

Leclère, Q., Pereira, A., Bailly, C., Antoni, J., Picard, C., 2017. A unified formalism for acoustic imaging based on microphone array measurements. Int. J. Aeroacoustics 16 (4–5), 431–456. http://dx.doi.org/10.1177/1475472X17718883.

Lesoinne, M., Sarkis, M., Hetmaniuk, U., Farhat, C., 2001. A linearized method for the frequency analysis of three-dimensional fluid/structure interaction problems in all flow regimes. Comput. Methods Appl. Mech. Engrg. 190 (24), 3121–3146. http://dx.doi.org/10.1016/S0045-7825(00)00385-6, Advances in Computational Methods for Fluid-Structure Interaction.

Leval, J., Picart, P., Boileau, J.P., Pascal, J.C., 2005. Full-field vibrometry with digital Fresnel holography. Appl. Opt. 44 (27), 5763–5772. http://dx.doi.org/10.1364/AO.44.005763.

Li, D., Da Ronch, A., Chen, G., Li, Y., 2019. Aeroelastic global structural optimization using an efficient CFD-based reduced order model. Aerosp. Sci. Technol. 94, 105354. http://dx.doi.org/10.1016/j.ast.2019.105354.

Li, D., Zhou, Q., Chen, G., Li, Y., 2017. Structural dynamic reanalysis method for transonic aeroelastic analysis with global structural modifications. J. Fluids Struct. 74, 306–320. http://dx.doi.org/10.1016/j.jfluidstructs.2017.06.004.

Liu, Y., Chen, Y., Shao, C., Alshamrani, A.M., 2024. The efficient data-driven solution to estimate the nonlinear bending of sandwich doubly curved panel subjected to transient loading. Aerosp. Sci. Technol. 147, 108980. http://dx.doi.org/10.1016/j.ast.2024.108980.

Liu, W., Ewins, D., 1999. The importance assessment of RDOF in FRF coupling analysis. In: Proceedings of the IMAC 17th Conference, Kissimmee, Florida. pp. 1481–1487, URL: https://citeseerx.ist.psu.edu/document?repid=rep1&type=pdf&doi=c44ebc7b37f462e47b44aee1acb1f9de704e92d6. Society for Experimental Mechanics (SEM).

Lokatt, M., 2017. Aeroelastic flutter analysis considering modeling uncertainties. J. Fluids Struct. 74, 247–262. http://dx.doi.org/10.1016/j.jfluidstructs.2017.06.017.

Lopes, H., Araújo dos Santos, J.V., Moreno-García, P., 2019. Evaluation of noise in measurements with speckle shearography. Mech. Syst. Signal Process. 118, 259–276. http://dx.doi.org/10.1016/j.ymssp.2018.08.042.

Lopes, H., Ferreira, F., Araújo dos Santos, J., Moreno-García, P., 2014. Localization of damage with speckle shearography and higher order spatial derivatives. Mech. Syst. Signal Process. 49 (1), 24–38. http://dx.doi.org/10.1016/j.ymssp.2013.12.016.

Maas, A.A.M., 1991. Phase Shifting Speckle Interferometry (Ph.D. thesis). Delft University Press.

Mas, P., Sas, P., 2004. Acoustic Source Identification Based on Microphone Array Processing. Tech. rep., Katholieke Universiteit Leuven, Belgium, Mechanical Engineering Department, Noise & Vibration Research Group, URL: https://www.mech.kuleuven.be/en/research/. In ISAAC 15 - Course on numerical and applied acoustics, Katholieke Universiteit Leuven, Belgium, Mechanical Engineering Department, Noise & Vibration research group, URL: https://www.isma-isaac.be.

Maynard, J.D., Williams, E.G., Lee, Y., 1985. Nearfield acoustic holography: I. Theory of generalized holography and the development of NAH. J. Acoust. Soc. Am. 78 (4), 1395–1413. http://dx.doi.org/10.1121/1.392911.

Mendez, C., Le Clainche, S., Moreno-Ramos, R., Vega, J.M., 2021. A new automatic, very efficient method for the analysis of flight flutter testing data. Aerosp. Sci. Technol. 114, 106749. http://dx.doi.org/10.1016/j.ast.2021.106749.

Meteyer, E., Montresor, S., Foucart, F., Le Meur, J., Heggarty, K., Pezerat, C., Picart, P., 2021. Lock-in vibration retrieval based on high-speed full-field coherent imaging. Sci. Rep. 11 (1), 15. http://dx.doi.org/10.1038/s41598-021-86371-3.

Mueller, T., Haeussler, M., Sedlmair, S., Rixen, D.J., 2020. Airborne transfer path analysis for an e-compressor. In: Proceedings of the ISMA2020 Including USD2020 - International Conference on Noise and Vibration Engineering, Leuven, Belgium, September 7-9. KU Leuven, pp. 3351–3364, URL: https://past.isma-isaac.be/downloads/isma2020/proceedings/Contribution_287_proceeding_3.pdf. Vehicle noise and vibration (NVH), paper ID 287.

Musella, U., D'Elia, G., Manzato, S., Peeters, B., Guillaume, P., Marulo, F., 2017. Analyses of target definition processes for MIMO random vibration control tests. In: Dervilis, N. (Ed.), Special Topics in Structural Dynamics, Volume 6. Springer International Publishing, Cham, pp. 135–148. http://dx.doi.org/10.1007/978-3-319-53841-9_12.

Ochoa, N.A., Marroquin, J., Dávila, A., 1999. Phase recovery using a twin-pulsed addition fringe pattern in ESPI. Opt. Commun. 163 (1), 15–19. http://dx.doi.org/10.1016/S0030-4018(99)00123-6.

O'Donoughue, P., Gautier, F., Meteyer, E., Durand-Texte, T., Secail-Geraud, M., Foucart, F., Robin, O., Berry, A., Melon, M., Pézerat, C., Pelat, A., Picart, P., 2023. Comparison of three full-field optical measurement techniques applied to vibration analysis. Sci. Rep. 13 (1), 22. http://dx.doi.org/10.1038/s41598-023-30053-9.

Ohayon, R., Soize, C., 2012. Advanced computational dissipative structural acoustics and fluid-structure interaction in low- and medium-frequency domains. Reduced-order models and uncertainty quantification. Int. J. Aeronaut. Space Sci. 13 (2), 127–153. http://dx.doi.org/10.5139/IJASS.2012.13.2.127.

Ortega Almirón, J., Bianciardi, F., Corbeels, P., Pieroni, N., Kindt, P., Desmet, W., 2022. Vehicle road noise prediction using component-based transfer path analysis from tire test-rig measurements on a rolling tire. J. Sound Vib. 523, 116694. http://dx.doi.org/10.1016/j.jsv.2021.116694.

Patil, H.H., Pitchaimani, J., 2024. Sound radiation characteristics of a beam under supersonic airflow and non-uniform temperature field. Aerosp. Sci. Technol. 147, 109001. http://dx.doi.org/10.1016/j.ast.2024.109001.

Pogacar, M., Ocepek, D., Trainotti, F., Cepon, G., Boltezar, M., 2022. System equivalent model mixing: A modal domain formulation. Mech. Syst. Signal Process. 177, 109239. http://dx.doi.org/10.1016/j.ymssp.2022.109239.

Rastogi, P.K., 1997. Optical Measurement Techniques and Applications. Artech House, Inc., Nordwood, MA 02062, U.S.A.

Research network, 1998. QUATTRO Brite-Euram Project no: BE 97-4184. Tech. rep., European Commision Research Framework Programs.

Richards, E.L., Song, H.C., Hodgkiss, W.S., 2018. Acoustic scattering comparison of Kirchhoff approximation to Rayleigh-Fourier method for sinusoidal surface waves at low grazing angles. J. Acoust. Soc. Am. 144 (3), 1269–1278. http://dx.doi.org/10.1121/1.5052256.

Sandberg, G., Wernberg, P.-A., Davidsson, P., 2009. Fundamentals of fluid-structure interaction. In: Computational Aspects of Structural Acoustics and Vibration. 505, Springer Vienna, Vienna, pp. 23–101. http://dx.doi.org/10.1007/978-3-211-89651-8_2.

Schreiber, H., Bruning, J.H., 2007. Phase shifting interferometry. In: Optical Shop Testing. John Wiley & Sons, Ltd, pp. 547–666. http://dx.doi.org/10.1002/9780470135976.ch14.

Schumann, C., Allen, M., Tuman, M., DeLima, W., Dodgen, E., 2022. Transmission simulator based MIMO response reconstruction. Exp. Tech. 46, 287–297. http://dx.doi.org/10.1007/s40799-021-00454-4.

Silva, G.C., Donadon, M.V., Silvestre, F.J., 2021. Experimental and numerical investigations on the nonlinear aeroelastic behavior of high aspect-ratio wings for different chord-wise store positions under stall and follower aerodynamic load models. Int. J. Non-Linear Mech. 131, 103685. http://dx.doi.org/10.1016/j.ijnonlinmec.2021.103685.

Squicciarini, G., Putra, A., Thompson, D.J., Zhang, X., Salim, M.A., 2015. Use of a reciprocity technique to measure the radiation efficiency of a vibrating structure. Appl. Acoust. 89, 107–121. http://dx.doi.org/10.1016/j.apacoust.2014.09.013.

Stanbridge, A.B., Ewins, D.J., 1999. Modal testing using a scanning laser doppler vibrometer. Mech. Syst. Signal Process. 13 (2), 255–270. http://dx.doi.org/10.1006/mssp.1998.1209.

Stanbridge, A.B., Martarelli, M., Ewins, D.J., 2004. Measuring area vibration mode shapes with a continuous-scan LDV. Measurement 35 (2), 181–189. http://dx.doi.org/10.1016/j.measurement.2003.07.005, 2 special issues: Vibration measurement by Laser techniques Advances and Applications and 7th workshop on ADC modelling and testing.

Steinbichler, H., Gehring, G., 1996. TV-holography and holographic interferometry: Industrial applications. Opt. Lasers Eng. 24 (2), 111–127. http://dx.doi.org/10.1016/0143-8166(95)00025-9, Civil and Structural Engineering Measurements with Interferometry, Shearography, and Holography.

Sutton, M.A., Orteu, J.J., Schreier, H., 2009. Image Correlation for Shape, Motion and Deformation Measurements: Basic Concepts, Theory and Applications. Springer US, http://dx.doi.org/10.1007/978-0-387-78747-3.

Takezawa, A., Daifuku, M., Nakano, Y., Nakagawa, K., Yamamoto, T., Kitamura, M., 2016. Topology optimization of damping material for reducing resonance response based on complex dynamic compliance. J. Sound Vib. 365, 230–243. http://dx.doi.org/10.1016/j.jsv.2015.11.045.

Tian, W., Gu, Y., Liu, H., Wang, X., Yang, Z., Li, Y., Li, P., 2021. Nonlinear aeroservoelastic analysis of a supersonic aircraft with control fin free-play by component mode synthesis technique. J. Sound Vib. 493, 115835. http://dx.doi.org/10.1016/j.jsv.2020.115835.

Tian, K., Wang, Y., Cao, D., Yu, K., 2024. Approximate global mode method for flutter analysis of folding wings. Int. J. Mech. Sci. 265, 108902. http://dx.doi.org/10.1016/j.ijmecsci.2023.108902.

Tsushima, N., Su, W., Gutierrez, H., Wolf, M.G., Griffin, E.D., Whittaker, J.T., Dumoulin, M.P., 2017. Monitoring multi-axial vibrations of flexible rockets using sensor-instrumented reference strain structures. Aerosp. Sci. Technol. 71, 285–298. http://dx.doi.org/10.1016/j.ast.2017.09.026.

Tsushima, N., Tamayama, M., Arizono, H., Makihara, K., 2021. Geometrically nonlinear aeroelastic characteristics of highly flexible wing fabricated by additive manufacturing. Aerosp. Sci. Technol. 117, 106923. http://dx.doi.org/10.1016/j.ast.2021.106923.

Vaes, D., Swevers, J., Sas, P., 2005. Experimental validation of different MIMO-feedback controller design methods. Control Eng. Pract. 13 (11), 1439–1451. http://dx.doi.org/10.1016/j.conengprac.2004.12.013.

Van der Auweraer, H., Dierckx, B., Haberstok, C., Freymann, R., et al., 1999. Structural modelling of car panels using holographic modal analysis. In: Proc. of the 1999 Noise and Vibration Conference, Traverse City (MI), USA. 3, pp. 1495–1506. http://dx.doi.org/10.4271/1999-01-1849, SAE P-342.

Van der Auweraer, H., Steinbichler, H., Haberstok, C., Freymann, R., Storer, D., 2000. Integration of pulsed-laser ESPI with spatial domain modal analysis: results from the SALOME project. In: Proc. of the 4th International Conference on Vibration Measurements By Laser Techniques: Advances and Applications. 4072, SPIE, pp. 313–322. http://dx.doi.org/10.1117/12.386741,

Van der Auweraer, H., Steinbichler, H., Haberstok, C., Freymann, R., Storer, D., Linet, V., 2001. Industrial applications of pulsed-laser ESPI vibration analysis. In: Proc. of the XIX IMAC, Kissimmee, FL, USA. SEM, pp. 490–496, URL: https://www.researchgate.net/publication/238246330_Industrial_Applications_of_Pulsed-Laser_ESPI_Vibration_Analysis.

Van der Auweraer, H., Steinbichler, H., Vanlanduit, S., Haberstok, C., Freymann, R., Storer, D., Linet, V., 2002. Application of stroboscopic and pulsed-laser electronic speckle pattern interferometry (ESPI) to modal analysis problems. Meas. Sci. Technol. 13, 451–463. http://dx.doi.org/10.1088/0957-0233/13/4/305.

Van der Auweraer, H., Mas, P., Peeters, P., Janssens, K., Vecchio, A., 2008. Modal and path contribution models from in-operation data: Review and new approaches. Shock. Vib. 15, http://dx.doi.org/10.1155/2008/632312.

van der Seijs, M.V., de Klerk, D., Rixen, D.J., 2016. General framework for transfer path analysis: History, theory and classification of techniques. Mech. Syst. Signal Process. 68–69, 217–244. http://dx.doi.org/10.1016/j.ymssp.2015.08.004.

van Hal, B., Desmet, W., Vandepitte, D., 2005. Hybrid finite element-wave-based method for steady-state interior structural-acoustic problems. Comput. Struct. 83 (2), 167–180. http://dx.doi.org/10.1016/j.compstruc.2004.04.019, Advances in Analysis of Fluid Structure Interaction.

Veronesi, W.A., Maynard, J.D., 1987. Nearfield acoustic holography (NAH) II. Holographic reconstruction algorithms and computer implementation. J. Acoust. Soc. Am. 81 (5), 1307–1322. http://dx.doi.org/10.1121/1.394536.

Vicente, W., Picelli, R., Pavanello, R., Xie, Y., 2015. Topology optimization of frequency responses of fluid–structure interaction systems. Finite Elem. Anal. Des. 98, 1–13. http://dx.doi.org/10.1016/j.finel.2015.01.009.

Voormeeren, S., de Klerk, D., Rixen, D., 2010. Uncertainty quantification in experimental frequency based substructuring. Mech. Syst. Signal Process. 24 (1), 106–118. http://dx.doi.org/10.1016/j.ymssp.2009.01.016.

Vrooman, H.A., 1991. Quantitative Analysis of Interferograms (Ph.D. thesis). Delft University Press.

Wagner, P., Huesmann, A.P., van der Seijs, M.V., 2020. Application of dynamic substructuring in NVH design of electric drivetrains. In: Proceedings of the ISMA2020 Including USD2020 - International Conference on Noise and Vibration Engineering, Leuven, Belgium, September 7-9. KU Leuven, pp. 3365–3382, URL: https://past.isma-isaac.be/downloads/isma2020/proceedings/Contribution_369_proceeding_3.pdf. Vehicle noise and vibration (NVH), paper ID 369.

Wang, W., Mottershead, J.E., Ihle, A., Siebert, T., Schubach, H.R., 2011a. Finite element model updating from full-field vibration measurement using digital image correlation. J. Sound Vib. 330 (8), 1599–1620. http://dx.doi.org/10.1016/j.jsv.2010.10.036.

Wang, W., Mottershead, J., Siebert, T., Pipino, A., 2011b. Frequency response functions of shape features from full-field vibration measurements using digital image correlation. Mech. Syst. Signal Process. 28, 333–347. http://dx.doi.org/10.1016/j.ymssp.2011.11.023, Elsevier Science Ltd.

Wang, X., Yang, Z., Zhou, S., Zhang, G., 2022. Complex damping influences on the oscillatory/static instability characteristics of heated panels in supersonic airflow. Mech. Syst. Signal Process. 165, 108369. http://dx.doi.org/10.1016/j.ymssp.2021.108369.

Warren, C., Niezrecki, C., Avitabile, P., Pingle, P., 2011. Comparison of FRF measurements and mode shapes determined using optically image based, laser, and accelerometer measurements. Mech. Syst. Signal Process. 25 (6), 2191–2202. http://dx.doi.org/10.1016/j.ymssp.2011.01.018, Interdisciplinary Aspects of Vehicle Dynamics.

Werter, N., De Breuker, R., 2016. A novel dynamic aeroelastic framework for aeroelastic tailoring and structural optimisation. Compos. Struct. 158, 369–386. http://dx.doi.org/10.1016/j.compstruct.2016.09.044.

Wikipedia.org, 2024a. Density of air. https://en.wikipedia.org/wiki/International_Standard_Atmosphere. (Accessed 02 May 2024).

Wikipedia.org, 2024b. Speed of sound. https://en.wikipedia.org/wiki/Speed_of_sound. (Accessed 02 May 2024).

Wikipedia.org, 2025. Colors of noise. https://en.wikipedia.org/wiki/Colors_of_noise. (Accessed 09 February 2025).

Williams, E.G., 1999. Fourier Acoustics: Sound Radiation and Nearfield Acoustical Holography. Elsevier Science, Amsterdam, The Netherlands, http://dx.doi.org/10.1016/B978-0-12-753960-7.X5000-1.

Wind, J., Wijnant, Y., de Boer, A., 2006. Fast evaluation of the Rayleigh integral and applications to inverse acoustics. In: Proceedings of the ICSV13, the Thirteenth International Congress on Sound and Vibration, Vienna, Austria, July 2-6, 2006. International Institute of Acoustics and Vibration (IIAV), pp. 1–8.

Wong, W., Chan, K., 1998. Quantitative vibration amplitude measurement with time-averaged digital speckle pattern interferometry. Opt. Laser Technol. 30 (5), 317–324. http://dx.doi.org/10.1016/S0030-3992(98)00059-0.

Wu, B., Wang, Q., Liao, H., Li, Y., Li, M., 2020. Flutter derivatives of a flat plate section and analysis of flutter instability at various wind angles of attack. J. Wind Eng. Ind. Aerodyn. 196, 104046. http://dx.doi.org/10.1016/j.jweia.2019.104046.

Xu, F., Yang, J., Zhang, M., Yu, H., 2021. Experimental investigations on post-flutter performance of a bridge deck sectional model using a novel testing device. J. Wind Eng. Ind. Aerodyn. 217, 104752. http://dx.doi.org/10.1016/j.jweia.2021.104752.

Zanarini, A., 2014a. On the estimation of frequency response functions, dynamic rotational degrees of freedom and strain maps from different full field optical techniques. In: Proceedings of the ISMA2014 Including USD2014 - International Conference on Noise and Vibration Engineering, Leuven, Belgium, September 15-17. KU Leuven, pp. 1177–1192, URL: http://past.isma-isaac.be/downloads/isma2014/papers/isma2014_0676.pdf. Dynamic testing: methods and instrumentation, paper ID676.

Zanarini, A., 2014b. On the role of spatial resolution in advanced vibration measurements for operational modal analysis and model updating. In: Proceedings of the ISMA2014 Including USD2014 - International Conference on Noise and Vibration Engineering, Leuven, Belgium, September 15-17. KU Leuven, pp. 3397–3410, URL: http://past.isma-isaac.be/downloads/isma2014/papers/isma2014_0678.pdf. Operational modal analysis, paper ID678.

Zanarini, A., 2018. Broad frequency band full field measurements for advanced applications: Point-wise comparisons between optical technologies. Mech. Syst. Signal Process. 98, 968–999. http://dx.doi.org/10.1016/j.ymssp.2017.05.035.

Zanarini, A., 2019a. Competing optical instruments for the estimation of Full Field FRFs. Measurement 140, 100–119. http://dx.doi.org/10.1016/j.measurement.2018.12.017.

Zanarini, A., 2019b. Full field optical measurements in experimental modal analysis and model updating. J. Sound Vib. 442, 817–842. http://dx.doi.org/10.1016/j.jsv.2018.09.048.

Zanarini, A., 2020. On the making of precise comparisons with optical full field technologies in NVH. In: ISMA2020 Including USD2020 - International Conference on Noise and Vibration Engineering, Leuven, Belgium, September 7-9. KU Leuven, pp. 2293–2308, URL: https://past.isma-isaac.be/downloads/isma2020/proceedings/Contribution_695_proceeding_3.pdf. Optical methods and computer vision for vibration engineering, paper ID 695.

Zanarini, A., 2022a. Chasing the high-resolution mapping of rotational and strain FRFs as receptance processing from different full-field optical measuring technologies. Mech. Syst. Signal Process. 166, 108428. http://dx.doi.org/10.1016/j.ymssp.2021.108428.

Zanarini, A., 2022b. Introducing the concept of defect tolerance by fatigue spectral methods based on full-field frequency response function testing and dynamic excitation signature. Int. J. Fatigue 165, 107184. http://dx.doi.org/10.1016/j.ijfatigue.2022.107184.

Zanarini, A., 2022c. On the approximation of sound radiation by means of experiment-based optical full-field receptances. In: ISMA2022 Including USD2022 - International Conference on Noise and Vibration Engineering, Leuven, Belgium, September 12-14. KU Leuven, pp. 2735–2749, URL: https://past.isma-isaac.be/downloads/isma2022/proceedings/Contribution_207_proceeding_3.pdf. paper ID 207 in Vol. Optical Methods.

Zanarini, A., 2023a. Experiment-based optical full-field receptances in the approximation of sound radiation from a vibrating plate. In: IMAC XLI - International Modal Analysis Conference - Keeping IMAC Weird: Traditional and Non-Traditional Applications of Structural Dynamics, Austin (Texas), USA. Springer Nature Switzerland AG & SEM Society for Experimental Mechanics, pp. 1–13. http://dx.doi.org/10.1007/978-3-031-34910-2_4, paper ID 14650 - chapter 4, in J. Baqersad, D. Di Maio (eds.), Computer Vision & Laser Vibrometry, Volume 6, Conference Proceedings of the Society for Experimental Mechanics Series.

Zanarini, A., 2023b. On the influence of scattered errors over full-field receptances in the Rayleigh integral approximation of sound radiation from a vibrating plate. Acoustics 5, 948–986. http://dx.doi.org/10.3390/acoustics5040055.

Zanarini, A., 2024a. On the use of full-field receptances in inverse vibro-acoustics for airborne structural dynamics. Procedia Struct. Integr. 54C, 107–114. http://dx.doi.org/10.1016/j.prostr.2024.01.062, paper ID 023@ICSI2023 The 5th International Conference on Structural Integrity, 28 August - 1 September, 2023.

Zanarini, A., 2024b. Mapping the defect acceptance for dynamically loaded components by exploiting DIC-based full-field receptances. Eng. Fail. Anal. 163, 108385. http://dx.doi.org/10.1016/j.engfailanal.2024.108385.

Zanarini, A., 2024c. Assessing the retrieval procedure of complex-valued forces from airborne pressure fields by means of DIC-based full-field receptances in simplified pseudo-inverse vibro-acoustics. Aerosp. Sci. Technol. 157, 109757. http://dx.doi.org/10.1016/j.ast.2024.109757.

Zanarini, A., 2025. Task-oriented structural health monitoring of dynamically loaded components by means of SLDV-based full-field mobilities and fatigue spectral methods. Appl. Sci. 15 (9), http://dx.doi.org/10.3390/app15094997.

Zhou, Q., feng Li, D., Da Ronch, A., Chen, G., ming Li, Y., 2016. Computational fluid dynamics-based transonic flutter suppression with control delay. J. Fluids Struct. 66, 183–206. http://dx.doi.org/10.1016/j.jfluidstructs.2016.07.002.